

# Precise predictions for the Higgs-boson decay

## $H \rightarrow WW/ZZ \rightarrow 4 \text{ leptons}$

A. BREDENSTEIN<sup>1</sup>, A. DENNER<sup>2</sup>, S. DITTMAIER<sup>1</sup> AND M.M. WEBER<sup>3</sup>

<sup>1</sup> *Max-Planck-Institut für Physik (Werner-Heisenberg-Institut),  
D-80805 München, Germany*

<sup>2</sup> *Paul Scherrer Institut, Würenlingen und Villigen,  
CH-5232 Villigen PSI, Switzerland*

<sup>3</sup> *Fachbereich Physik, Bergische Universität Wuppertal,  
D-42097 Wuppertal, Germany*

### Abstract:

The decay of the Standard Model Higgs boson into four leptons via a virtual W-boson or Z-boson pair is one of the most important decay modes in the Higgs-boson search at the LHC. We present the complete electroweak radiative corrections of  $\mathcal{O}(\alpha)$  to these processes, including improvements beyond  $\mathcal{O}(\alpha)$  originating from heavy-Higgs effects and final-state radiation. The intermediate W- and Z-boson resonances are described (without any expansion or on-shell approximation) by consistently employing complex mass parameters for the gauge bosons (complex-mass scheme). The corrections to partial decay widths typically amount to some per cent and increase with growing Higgs mass  $M_H$ , reaching about 8% at  $M_H \sim 500 \text{ GeV}$ . For not too large Higgs masses ( $M_H \lesssim 400 \text{ GeV}$ ) the corrections to the partial decay widths can be reproduced within  $\lesssim 2\%$  by simple approximations. For angular distributions the corrections are somewhat larger and distort the shapes. For invariant-mass distributions of fermion pairs they can reach several tens of per cent depending on the treatment of photon radiation. The discussed corrections have been implemented in a Monte Carlo event generator called PROPHECY4F.<sup>†</sup>

March 2006

---

<sup>†</sup>The computer code can be obtained from the authors upon request.

## 1 Introduction

The primary task of the LHC will be the detection and the study of the Higgs boson. If it is heavier than 140 GeV and behaves as predicted by the Standard Model (SM), it decays predominantly into gauge-boson pairs and subsequently into four light fermions. From a Higgs-boson mass  $M_H$  of about 130 GeV up to the Z-boson-pair threshold  $2M_Z$ , the decay signature  $H(\rightarrow WW) \rightarrow 2 \text{ leptons} + \text{missing } p_T$  [ 1, 2] has the highest discovery potential for the Higgs boson at the LHC [ 3]. For higher Higgs masses, the leading role is taken over by the “gold-plated” channel  $H \rightarrow ZZ \rightarrow 4 \text{ leptons}$ , which will allow for the most accurate measurement of  $M_H$  above 130 GeV [ 4]. More details and recent developments concerning Higgs studies at the LHC can be found in the literature [ 5, 6, 7]. At a future  $e^+e^-$  linear collider [ 8, 9, 10], the decays  $H \rightarrow 4f$  will enable measurements of the  $H \rightarrow WW/ZZ$  branching ratios at the level of a few to 10% [ 11].

A kinematical reconstruction of the Higgs boson and of the virtual W and Z bosons requires the study of distributions defined from the kinematics of the decay fermions. Thereby, it is important to include radiative corrections, in particular real photon radiation. In addition, the verification of the spin and of the CP properties of the Higgs boson relies on the study of angular, energy, and invariant-mass distributions [ 12, 13]. In particular, the sensitivity of the angle between the two Z-decay planes in  $H \rightarrow ZZ \rightarrow 4 \text{ leptons}$  has been frequently emphasized in the literature. As a consequence a Monte Carlo generator for  $H \rightarrow WW/ZZ \rightarrow 4 \text{ fermions}$  including all relevant corrections is needed.

The theoretical description of the decays of a SM Higgs boson into W- or Z-boson pairs started with lowest-order formulas for the partial decay widths. The first calculations [ 14] that include off-shell effects of the gauge bosons made the approximation that one of the W or Z bosons was still on shell, an approximation that turns out to be not sufficient. Later calculations [ 15] dealt with the situation of two intermediate off-shell gauge bosons. The various approaches are compared, e.g., in Ref. [ 16]. We note that the program HDECAY [ 17], which is frequently used in practice, calculates the partial decay widths for  $H \rightarrow WW/ZZ$  with on- or off-shell gauge bosons depending on  $M_H$ . Distributions of the decay fermions have been considered in Refs. [ 12, 13], but still in lowest order of perturbation theory.

In the past the electroweak  $\mathcal{O}(\alpha)$  corrections to decays into gauge bosons,  $H \rightarrow WW/ZZ$ , were known [ 18, 19] only in narrow-width approximation (NWA), i.e. for on-shell W and Z bosons. In this case, also leading two-loop corrections enhanced by powers of the top-quark mass [ 20, 21] or of the Higgs-boson mass [ 22, 23] have been calculated. However, near and below the gauge-boson-pair thresholds the NWA is not applicable, so that only the lowest-order results exist in this  $M_H$  range. Recently electroweak corrections to the processes  $H \rightarrow WW/ZZ \rightarrow 4f$  with off-shell gauge bosons have been considered. Progress on a calculation of the electromagnetic corrections to  $H \rightarrow ZZ \rightarrow 4 \text{ leptons}$  has been reported at the RADCOR05 conference by Carloni Calame [ 24]. There we have also presented first results of our calculation of the complete  $\mathcal{O}(\alpha)$  corrections to the general  $H \rightarrow 4 \text{ leptons}$  processes [ 25].

In this paper we describe the details of our calculation of the  $\mathcal{O}(\alpha)$  corrections and of the included improvements beyond this order. The involved Feynman diagrams are closely related to the ones of the production process  $e^+e^- \rightarrow \nu\bar{\nu}H$ , whose electroweak

$\mathcal{O}(\alpha)$  corrections have been evaluated in Refs. [26, 27]. Therefore, we proceed in the algebraic reduction of the one-loop diagrams as described in Ref. [27]. On the other hand, the resonance structure of the decays  $H \rightarrow WW/ZZ \rightarrow 4f$  is practically the same as in  $e^+e^- \rightarrow WW \rightarrow 4f$ , which was treated at the one-loop level in Ref. [28]. Thus, we apply the “complex-mass scheme” [28, 29], where gauge-boson masses are consistently treated as complex quantities. This procedure fully maintains gauge invariance at the price of having complex gauge-boson masses everywhere, i.e. also in couplings and loop integrals. For a numerically stable evaluation of the latter we employ the methods described in Refs. [30, 31]. The combination of virtual and real photon corrections is performed in the dipole subtraction approach [32, 33] and checked by the alternative of phase-space slicing. The whole calculation has been implemented in a Monte Carlo generator called PROPHECY4F.

The paper is organized as follows. In Section 2 we fix our conventions and give explicit results for the tree-level amplitudes of the processes  $H \rightarrow WW/ZZ \rightarrow 4f$ . Section 3 contains a description of our calculation of the virtual one-loop corrections; the real photon corrections are considered in Section 4. Some details on the employed Monte Carlo techniques are given in Section 5. In Section 6 we construct an “improved Born approximation” (IBA) which approximates our state-of-the-art prediction for partial decay widths within  $\lesssim 2\%$  for not too large Higgs masses,  $M_H \lesssim 400 \text{ GeV}$ . Our numerical results are discussed in Section 7, comprising partial decay widths of several representative  $H \rightarrow WW/ZZ \rightarrow 4l$  channels as well as differential cross sections for selected channels in invariant masses of lepton pairs and in various angles. A comparison with results obtained from HDECAY for the partial widths is also performed there. Section 8 contains our conclusions.

## 2 Conventions and lowest-order results

We consider the lowest-order processes

$$H(p) \longrightarrow f_1(k_1, \sigma_1) + \bar{f}_2(k_2, \sigma_2) + f_3(k_3, \sigma_3) + \bar{f}_4(k_4, \sigma_4), \quad (2.1)$$

where the momenta and helicities of the external particles are indicated in parentheses. The helicities take the values  $\sigma_i = \pm 1/2$ , but we often use only the sign to indicate the helicity. The masses of the external fermions are neglected whenever possible; they are only taken into account in the mass-singular logarithms originating from collinear final-state radiation (FSR). The matrix elements can be constructed from the generic diagram shown in Figure 1.

Using the conventions of Refs. [34, 35] we denote the relevant couplings in the following by

$$\begin{aligned} g_{\gamma ff}^\pm &= -Q_f, & g_{Zff}^+ &= -\frac{s_w}{c_w} Q_f, & g_{Zff}^- &= -\frac{s_w}{c_w} Q_f + \frac{I_{w,f}^3}{c_w s_w}, \\ g_{Wff'}^- &= \frac{1}{\sqrt{2}s_w}, & g_{Wff'}^+ &= 0, \\ g_{HZZ} &= \frac{\mu_W}{c_w^2 s_w}, & g_{HWW} &= \frac{\mu_W}{s_w}, \end{aligned} \quad (2.2)$$

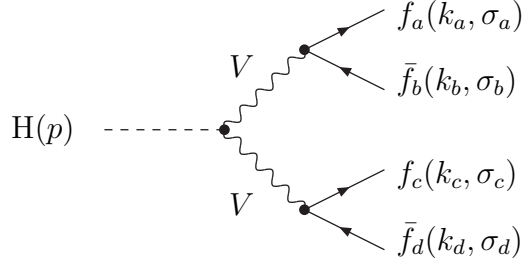


Figure 1: Generic lowest-order diagram for  $H \rightarrow 4f$  where  $V = W, Z$ .

where  $Q_f$  is the relative charge of the fermion  $f$ , and  $I_{w,f}^3 = \pm 1/2$  the third component of the weak isospin of the left-handed part of the fermion field  $f$ . The CKM matrix has been consistently set to the unit matrix, which has no sizeable effects on our results. In (2.2) we have already indicated that we use complex gauge-boson masses  $\mu_V$  everywhere,

$$\mu_V^2 = M_V^2 - iM_V\Gamma_V, \quad V = W, Z, \quad (2.3)$$

where  $M_V$  and  $\Gamma_V$  denote the real pole-mass and width parameters. Accordingly the sine and cosine of the weak mixing angle are fixed by

$$c_w^2 = 1 - s_w^2 = \frac{\mu_W^2}{\mu_Z^2}, \quad (2.4)$$

i.e.  $c_w$  and  $s_w$  are complex quantities. More details about the complex-mass scheme are given in Section 3.2.2.

In order to express the amplitudes in a compact way, we use the Weyl–van der Waerden (WvdW) spinor technique as formulated in Ref. [36]. The spinor products  $\langle \dots \rangle$  are defined by

$$\langle pq \rangle = \epsilon^{AB} p_A q_B = 2\sqrt{p_0 q_0} \left[ e^{-i\phi_p} \cos \frac{\theta_p}{2} \sin \frac{\theta_q}{2} - e^{-i\phi_q} \cos \frac{\theta_q}{2} \sin \frac{\theta_p}{2} \right], \quad (2.5)$$

where  $p_A, q_A$  are the associated momentum spinors for the light-like momenta

$$\begin{aligned} p^\mu &= p_0(1, \sin \theta_p \cos \phi_p, \sin \theta_p \sin \phi_p, \cos \theta_p), \\ q^\mu &= q_0(1, \sin \theta_q \cos \phi_q, \sin \theta_q \sin \phi_q, \cos \theta_q). \end{aligned} \quad (2.6)$$

In the notation of Ref. [36] the generic lowest-order amplitude reads

$$\mathcal{M}_0^{VV, \sigma_a \sigma_b \sigma_c \sigma_d}(k_a, k_b, k_c, k_d) = 2e^3 g_{Vf_a f_b}^{\sigma_a} g_{Vf_c f_d}^{\sigma_c} g_{HVV} \delta_{\sigma_a, -\sigma_b} \delta_{\sigma_c, -\sigma_d} A_{\sigma_a \sigma_c}^{VV}(k_a, k_b, k_c, k_d), \quad (2.7)$$

or more specifically for the case of Z-mediated and W-mediated decays

$$\begin{aligned} \mathcal{M}_0^{ZZ, \sigma_a \sigma_b \sigma_c \sigma_d}(k_a, k_b, k_c, k_d) &= \frac{2e^3 g_{Zf_a f_b}^{\sigma_a} g_{Zf_c f_d}^{\sigma_c} \mu_W}{c_w^2 s_w} \delta_{\sigma_a, -\sigma_b} \delta_{\sigma_c, -\sigma_d} A_{\sigma_a \sigma_c}^{ZZ}(k_a, k_b, k_c, k_d), \\ \mathcal{M}_0^{WW, \sigma_a \sigma_b \sigma_c \sigma_d}(k_a, k_b, k_c, k_d) &= \frac{e^3 \mu_W}{s_w^3} \delta_{\sigma_a, -} \delta_{\sigma_b, +} \delta_{\sigma_c, -} \delta_{\sigma_d, +} A_{--}^{WW}(k_a, k_b, k_c, k_d). \end{aligned} \quad (2.8)$$

The auxiliary functions are given by

$$\begin{aligned}
A_{--}^{VV}(k_a, k_b, k_c, k_d) &= \frac{\langle k_b k_d \rangle^* \langle k_a k_c \rangle}{[(k_a + k_b)^2 - \mu_V^2][(k_c + k_d)^2 - \mu_V^2]}, \\
A_{+-}^{VV}(k_a, k_b, k_c, k_d) &= A_{--}^{VV}(k_b, k_a, k_c, k_d), \\
A_{-+}^{VV}(k_a, k_b, k_c, k_d) &= A_{--}^{VV}(k_a, k_b, k_d, k_c), \\
A_{++}^{VV}(k_a, k_b, k_c, k_d) &= A_{--}^{VV}(k_b, k_a, k_d, k_c),
\end{aligned} \tag{2.9}$$

and obey the relations

$$\begin{aligned}
A_{-\sigma_a, -\sigma_c}^{VV}(k_a, k_b, k_c, k_d) &= \left( A_{\sigma_a \sigma_c}^{VV}(k_a, k_b, k_c, k_d) \right)^* \Big|_{\mu_V \rightarrow \mu_V^*}, \\
A_{-\sigma_a, \sigma_c}^{VV}(k_a, k_b, k_c, k_d) &= A_{\sigma_a \sigma_c}^{VV}(k_b, k_a, k_c, k_d), \\
A_{\sigma_a, -\sigma_c}^{VV}(k_a, k_b, k_c, k_d) &= A_{\sigma_a \sigma_c}^{VV}(k_a, k_b, k_d, k_c), \\
A_{\sigma_a \sigma_c}^{VV}(k_a, k_b, k_c, k_d) &= \left( A_{\sigma_a \sigma_c}^{VV}(k_b, k_a, k_d, k_c) \right)^* \Big|_{\mu_V \rightarrow \mu_V^*}, \\
A_{\sigma_c \sigma_a}^{VV}(k_a, k_b, k_c, k_d) &= A_{\sigma_c \sigma_a}^{VV}(k_c, k_d, k_a, k_b).
\end{aligned} \tag{2.10}$$

The relations between the  $A_{\dots}$  functions that differ in all helicities result from a P transformation. Those where only one fermion helicity is reversed are related to C symmetry. The last but one is due to CP symmetry, and the last one results from a symmetry under the exchange of the two fermion pairs. The replacements  $\mu_V \rightarrow \mu_V^*$  in (2.10) ensure that the vector-boson masses remain unaffected by complex conjugation.

From the generic matrix element  $\mathcal{M}_0^{VV, \sigma_a \sigma_b \sigma_c \sigma_d}(k_a, k_b, k_c, k_d)$  the matrix elements for the specific processes can be constructed as follows. To write down the explicit matrix elements for the different final states, we denote different fermions ( $f \neq F$ ) by  $f$  and  $F$ , and their weak-isospin partners by  $f'$  and  $F'$ , respectively:

- $H \rightarrow f \bar{f} F \bar{F}$ :

$$\mathcal{M}_0^{\sigma_1 \sigma_2 \sigma_3 \sigma_4}(k_1, k_2, k_3, k_4) = \mathcal{M}_0^{ZZ, \sigma_1 \sigma_2 \sigma_3 \sigma_4}(k_1, k_2, k_3, k_4), \tag{2.11}$$

- $H \rightarrow f \bar{f}' F \bar{F}'$ :

$$\mathcal{M}_0^{\sigma_1 \sigma_2 \sigma_3 \sigma_4}(k_1, k_2, k_3, k_4) = \mathcal{M}_0^{WW, \sigma_1 \sigma_2 \sigma_3 \sigma_4}(k_1, k_2, k_3, k_4), \tag{2.12}$$

- $H \rightarrow f \bar{f} f \bar{f}$ :

$$\begin{aligned}
\mathcal{M}_0^{\sigma_1 \sigma_2 \sigma_3 \sigma_4}(k_1, k_2, k_3, k_4) &= \mathcal{M}_0^{ZZ, \sigma_1 \sigma_2 \sigma_3 \sigma_4}(k_1, k_2, k_3, k_4) \\
&\quad - \mathcal{M}_0^{ZZ, \sigma_1 \sigma_4 \sigma_3 \sigma_2}(k_1, k_4, k_3, k_2),
\end{aligned} \tag{2.13}$$

- $H \rightarrow f \bar{f} f' \bar{f}'$ :

$$\begin{aligned}
\mathcal{M}_0^{\sigma_1 \sigma_2 \sigma_3 \sigma_4}(k_1, k_2, k_3, k_4) &= \mathcal{M}_0^{ZZ, \sigma_1 \sigma_2 \sigma_3 \sigma_4}(k_1, k_2, k_3, k_4) \\
&\quad - \mathcal{M}_0^{WW, \sigma_1 \sigma_4 \sigma_3 \sigma_2}(k_1, k_4, k_3, k_2).
\end{aligned} \tag{2.14}$$

The relative signs between contributions of the basic subamplitudes to the full matrix elements account for the sign changes resulting from interchanging external fermion lines.

The matrix elements of (2.11) and (2.12) can be extended to the case of semi-leptonic or hadronic final states by simply multiplying the squared matrix element by a colour factor 3 or 9, respectively. On the other hand, care has to be taken in the cases of (2.13) and (2.14) for hadronic final states (semi-leptonic final states do not exist) owing to the non-trivial colour interferences. Summing over the colour degrees of freedom, we have

- $H \rightarrow q\bar{q}q\bar{q}$ :

$$|\mathcal{M}_0^{\sigma_1\sigma_2\sigma_3\sigma_4}(k_1, k_2, k_3, k_4)|^2 = 9 \left| \mathcal{M}_0^{ZZ, \sigma_1\sigma_2\sigma_3\sigma_4}(k_1, k_2, k_3, k_4) \right|^2 + 9 \left| \mathcal{M}_0^{ZZ, \sigma_1\sigma_4\sigma_3\sigma_2}(k_1, k_4, k_3, k_2) \right|^2 - 6 \operatorname{Re} \left\{ \mathcal{M}_0^{ZZ, \sigma_1\sigma_2\sigma_3\sigma_4}(k_1, k_2, k_3, k_4) \left( \mathcal{M}_0^{ZZ, \sigma_1\sigma_4\sigma_3\sigma_2}(k_1, k_4, k_3, k_2) \right)^* \right\}, \quad (2.15)$$

- $H \rightarrow q\bar{q}q'\bar{q}'$ :

$$|\mathcal{M}_0^{\sigma_1\sigma_2\sigma_3\sigma_4}(k_1, k_2, k_3, k_4)|^2 = 9 \left| \mathcal{M}_0^{ZZ, \sigma_1\sigma_2\sigma_3\sigma_4}(k_1, k_2, k_3, k_4) \right|^2 + 9 \left| \mathcal{M}_0^{WW, \sigma_1\sigma_4\sigma_3\sigma_2}(k_1, k_4, k_3, k_2) \right|^2 - 6 \operatorname{Re} \left\{ \mathcal{M}_0^{ZZ, \sigma_1\sigma_2\sigma_3\sigma_4}(k_1, k_2, k_3, k_4) \left( \mathcal{M}_0^{WW, \sigma_1\sigma_4\sigma_3\sigma_2}(k_1, k_4, k_3, k_2) \right)^* \right\}. \quad (2.16)$$

Here  $q$  denotes any quark of the first two generations and  $q'$  its weak-isospin partner.

Having constructed the matrix elements, we can write the lowest-order decay width  $\Gamma_0$  as

$$\int d\Gamma_0 = \frac{1}{2M_H} \int d\Phi_0 \sum_{\sigma_1, \sigma_2, \sigma_3, \sigma_4 = \pm \frac{1}{2}} |\mathcal{M}_0^{\sigma_1\sigma_2\sigma_3\sigma_4}|^2, \quad (2.17)$$

where the phase-space integral is defined by

$$\int d\Phi_0 = \left( \prod_{i=1}^4 \int \frac{d^3\mathbf{k}_i}{(2\pi)^3 2k_i^0} \right) (2\pi)^4 \delta^{(4)} \left( p - \sum_{j=1}^4 k_j \right). \quad (2.18)$$

For the case  $H \rightarrow f\bar{f}f\bar{f}$ , which involves two pairs of identical particles in the final state, we implicitly include a factor 1/4 in the phase-space integral, without making this factor explicit in the formulas.

### 3 Virtual corrections

#### 3.1 Survey of one-loop diagrams

The virtual corrections receive contributions from self-energy, vertex, box, and pentagon diagrams. The structural diagrams containing the generic contributions of vertex functions are summarized in Figure 2. Here and in the following we omit all diagrams that vanish in the limit of vanishing external fermion masses from the beginning. For charged-current processes the generic field  $V$  stands for the W-boson field, for neutral-current processes we have  $V = Z, \gamma$ , where the photon is absent in couplings to the Higgs

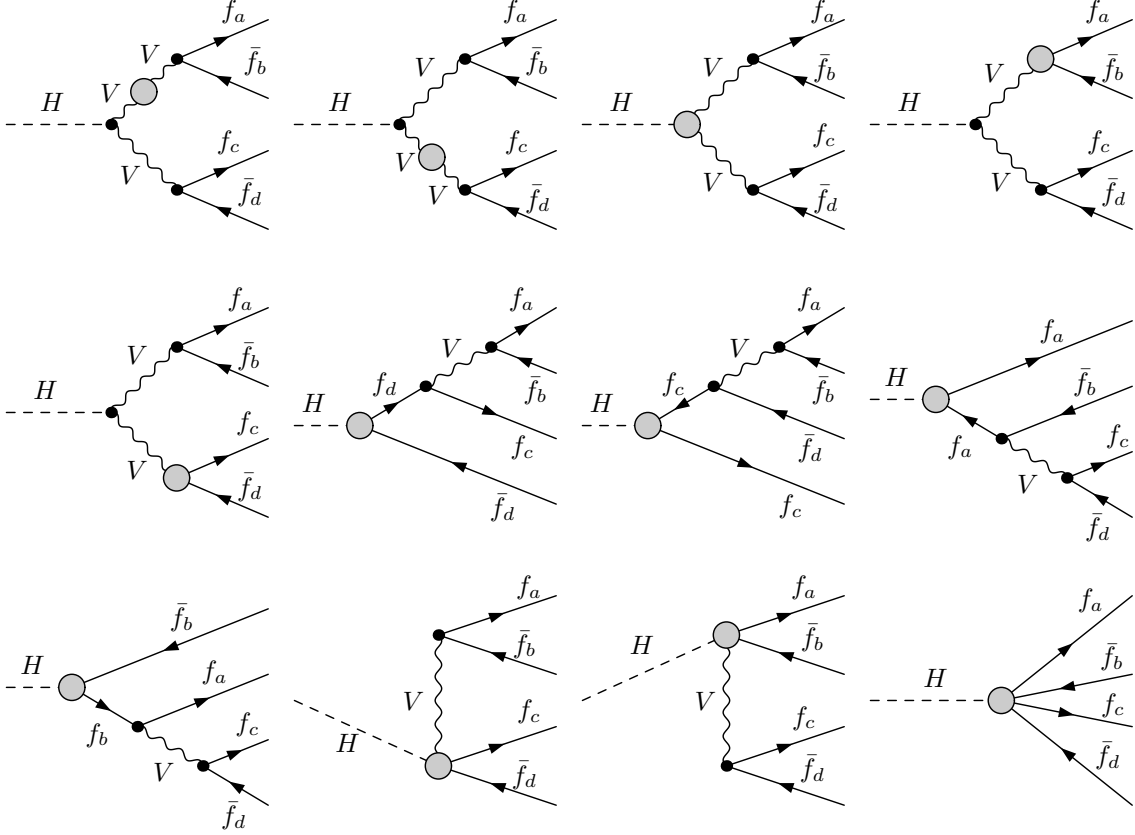


Figure 2: Generic contributions of different vertex functions to  $H \rightarrow WW/ZZ \rightarrow 4f$ , where the blobs stand for one-particle-irreducible one-loop vertex functions.

boson. The generic diagrams cover all structures relevant for electroweak corrections to arbitrary four-fermion final states, including quarks. Note, however, that some four-quark final states receive corrections from diagrams with intermediate gluons on tree-like lines (quark-loop-induced Hgg vertex). Possible QCD corrections for quarks in the final state will not be considered in the following lists of diagrams.

The pentagon diagrams are shown in Figures 3 and 4, respectively. The specific subdiagrams of loop-induced 4-point functions have been shown in Ref. [27], where the process class  $e^+e^- \rightarrow \nu\bar{\nu}H$  was analyzed at one loop. They involve 4-point vertex functions of the type  $\nu_l\bar{\nu}_lZH$ ,  $\nu_l\bar{\nu}_l\gamma H$ ,  $l^-l^+ZH$ ,  $l^-l^+\gamma H$ , and  $l^\pm(\bar{\nu}_l^{(\pm)})W^\pm H$  with  $l = e, \mu, \tau$  denoting any charged lepton. The diagrams for the  $l^-l^+\gamma H$  vertex function can be obtained from those for the  $l^-l^+ZH$  vertex function by replacing the external Z boson by a photon and omitting the diagram where the photon couples to neutrinos. The 3-point loop insertions in the  $H\nu_l\bar{\nu}_l$ ,  $Hl^-l^+$ ,  $HWW$ ,  $HZZ$ , and  $HZ\gamma$  vertices have also been listed in Ref. [27]; the one-loop diagrams for the  $H\gamma\gamma$  vertex follow from the  $HZZ$  or  $HZ\gamma$  case by obvious substitutions and omissions. Most of the diagrams for the self-energies and the  $\nu_l\bar{\nu}_lZ$ ,  $l^-l^+Z$ , and  $l^\pm(\bar{\nu}_l^{(\pm)})W^\pm$  vertex functions can be found in Ref. [37].

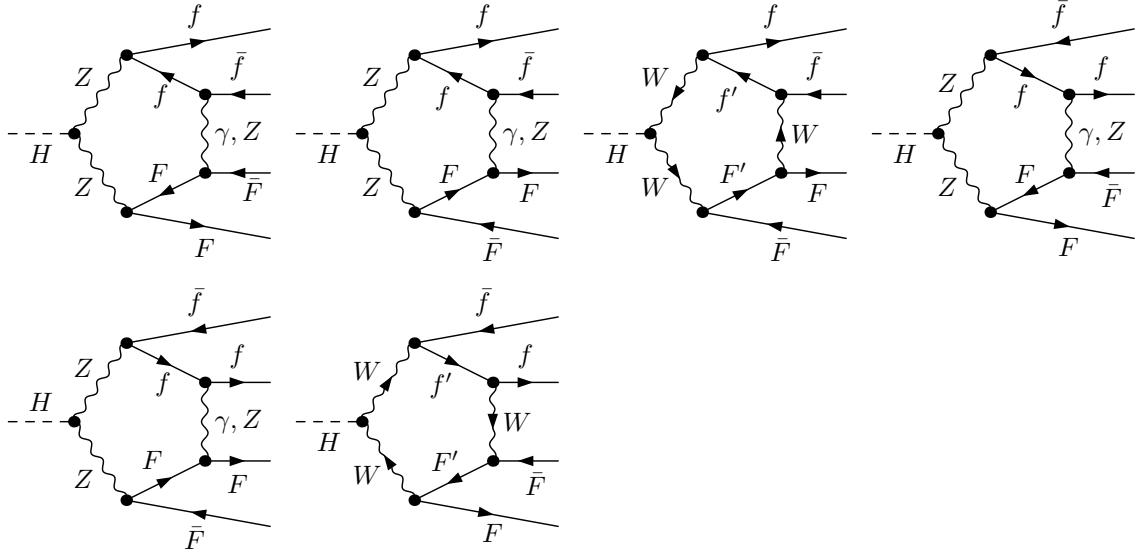


Figure 3: Pentagon diagrams for  $H \rightarrow ZZ \rightarrow f \bar{f} F \bar{F}$ , where  $f$  and  $F$  are different fermions with respective weak-isospin partners  $f'$  and  $F'$ . The fermion arrows in the diagrams involving  $W$  bosons apply to the case where both  $f$  and  $F$  have weak isospin  $I_{w,f}^3 = +1/2$ ; for fermions with  $I_{w,f}^3 = -1/2$  the corresponding fermion arrows have to be reversed.

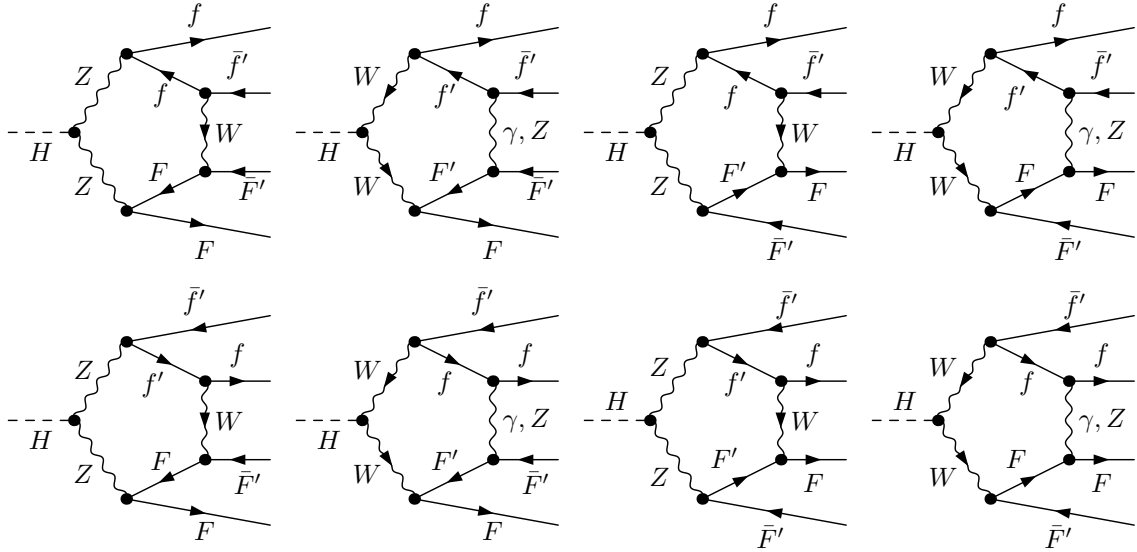


Figure 4: Pentagon diagrams for  $H \rightarrow WW \rightarrow f \bar{f} F \bar{F}$ , where  $f$  and  $F$  are different fermions with respective weak-isospin partners  $f'$  and  $F'$ . The fermion arrows apply to the case where  $f$  and  $F$  have weak isospin  $I_{w,f}^3 = +1/2$  and  $I_{w,F}^3 = -1/2$ , respectively; for fermions with opposite weak isospin the corresponding fermion arrows have to be reversed.



All pentagon and box diagrams as well as the  $H\gamma\gamma$  vertex function are UV finite; also the  $H\nu_l\bar{\nu}_l$  and  $Hl^+l^-$  vertex functions are UV finite since we neglect the masses of the light fermions everywhere apart from the mass-singular logarithms. For the other vertex functions, HWW, HZZ,  $HZ\gamma$ ,  $\nu_l\bar{\nu}_l Z$ ,  $l^-l^+Z$ ,  $l^\pm(\bar{\nu}_l)W^\mp$ , and for the relevant self-energies the corresponding counterterm diagrams have to be included.

### 3.2 Calculation of the one-loop corrections

#### 3.2.1 Algebraic reduction of diagrams and standard matrix elements

The algebraic part of the two calculations has been carried out in the same way as in the one-loop calculation of  $e^+e^- \rightarrow \nu\bar{\nu}H$  described in Ref. [27]. This means that we separate the fermion spinor chains from the rest of the amplitude by defining standard matrix elements (SME). To introduce a compact notation for the SME, the tensors

$$\begin{aligned}\Gamma_{\{\alpha,\alpha\beta\gamma\}}^{ab,\sigma} &= \bar{u}_{f_a}(k_a) \{\gamma_\alpha, \gamma_\alpha\gamma_\beta\gamma_\gamma\} \omega_\sigma v_{\bar{f}_b}(k_b), \\ \Gamma_{\{\alpha,\alpha\beta\gamma\}}^{cd,\tau} &= \bar{u}_{f_c}(k_c) \{\gamma_\alpha, \gamma_\alpha\gamma_\beta\gamma_\gamma\} \omega_\tau v_{\bar{f}_d}(k_d)\end{aligned}\quad (3.1)$$

are defined with obvious notations for the Dirac spinors  $\bar{u}_{f_a}(k_a)$ , etc., and  $\omega_\pm = (1 \pm \gamma_5)/2$  denote the right- and left-handed chirality projectors. Here and in the following, each entry in the set within curly brackets refers to a single object, i.e. from the first line in the equation above we have  $\Gamma_\alpha^{ab,\sigma} = \bar{u}_{f_a}(k_a)\gamma_\alpha\omega_\sigma v_{\bar{f}_b}(k_b)$  and  $\Gamma_{\alpha\beta\gamma}^{ab,\sigma} = \bar{u}_{f_a}(k_a)\gamma_\alpha\gamma_\beta\gamma_\gamma\omega_\sigma v_{\bar{f}_b}(k_b)$ , etc. Furthermore, symbols like  $\Gamma_p$  are used as shorthand for the contraction  $\Gamma_\mu p^\mu$ . We define the 52 SME

$$\begin{aligned}\hat{\mathcal{M}}_{\{1,2\}}^{abcd,\sigma\tau} &= \Gamma_\alpha^{ab,\sigma} \Gamma^{cd,\tau,\{\alpha,\alpha k_a k_b\}}, & \hat{\mathcal{M}}_{\{3,4\}}^{abcd,\sigma\tau} &= \Gamma_{\alpha k_c k_d}^{ab,\sigma} \Gamma^{cd,\tau,\{\alpha,\alpha k_a k_b\}}, \\ \hat{\mathcal{M}}_{\{5,6\}}^{abcd,\sigma\tau} &= \Gamma_{k_c}^{ab,\sigma} \Gamma^{cd,\tau,\{k_a, k_b\}}, & \hat{\mathcal{M}}_{\{7,8\}}^{abcd,\sigma\tau} &= \Gamma_{k_d}^{ab,\sigma} \Gamma^{cd,\tau,\{k_a, k_b\}}, \\ \hat{\mathcal{M}}_{\{9,10\}}^{abcd,\sigma\tau} &= \Gamma_{\alpha\beta k_c}^{ab,\sigma} \Gamma^{cd,\tau,\{\alpha\beta k_a, \alpha\beta k_b\}}, & \hat{\mathcal{M}}_{\{11,12\}}^{abcd,\sigma\tau} &= \Gamma_{\alpha\beta k_d}^{ab,\sigma} \Gamma^{cd,\tau,\{\alpha\beta k_a, \alpha\beta k_b\}}, \\ \hat{\mathcal{M}}_{13}^{abcd,\sigma\tau} &= \Gamma_{\alpha\beta\gamma}^{ab,\sigma} \Gamma^{cd,\tau,\alpha\beta\gamma}.\end{aligned}\quad (3.2)$$

The SME are evaluated within the WvdW spinor technique, similar to the lowest-order amplitudes described in the previous section. The tree-level and one-loop amplitudes  $\mathcal{M}_0^{abcd,\sigma\tau}$  and  $\mathcal{M}_1^{abcd,\sigma\tau}$ , respectively, for the generic four-fermion final state  $f_a\bar{f}_b f_c\bar{f}_d$  can be expanded in terms of linear combinations of SME,

$$\mathcal{M}_n^{abcd,\sigma\tau} = \sum_{i=1}^{13} F_{n,i}^{abcd,\sigma\tau} \hat{\mathcal{M}}_i^{abcd,\sigma\tau}, \quad n = 0, 1, \quad (3.3)$$

with Lorentz-invariant functions  $F_{n,i}^{abcd,\sigma\tau}$ . In this notation the lowest-order amplitudes (2.8) read

$$\begin{aligned}\mathcal{M}_0^{ZZ,\sigma_a\sigma_b\sigma_c\sigma_d}(k_a, k_b, k_c, k_d) &= \frac{e^3 g_{Zf_a f_b}^{\sigma_a} g_{Zf_c f_d}^{\sigma_c} \mu_W}{c_W^2 s_W} \delta_{\sigma_a, -\sigma_b} \delta_{\sigma_c, -\sigma_d} \\ &\quad \times \frac{1}{[(k_a + k_b)^2 - \mu_Z^2][(k_c + k_d)^2 - \mu_Z^2]} \hat{\mathcal{M}}_1^{abcd,\sigma_a\sigma_c},\end{aligned}$$

$$\mathcal{M}_0^{\text{WW},\sigma_a\sigma_b\sigma_c\sigma_d}(k_a, k_b, k_c, k_d) = \frac{e^3\mu_W}{2s_W^3} \delta_{\sigma_a,-}\delta_{\sigma_b,+}\delta_{\sigma_c,-}\delta_{\sigma_d,+} \times \frac{1}{[(k_a + k_b)^2 - \mu_W^2][(k_c + k_d)^2 - \mu_W^2]} \hat{\mathcal{M}}_1^{abcd,--}. \quad (3.4)$$

For the one-loop amplitudes in general all invariant functions receive contributions, in particular, they contain the loop integrals. The one-loop amplitudes for the various final states are constructed from the amplitudes for  $H \rightarrow f\bar{f}F\bar{F}$  and  $H \rightarrow f\bar{f}'F\bar{F}'$  as described in (2.11) to (2.14) for the lowest order. The one-loop correction to the partial decay widths, finally, reads

$$\int d\Gamma_{\text{virt}} = \frac{1}{2M_H} \int d\Phi_0 \sum_{\sigma_1,\sigma_2,\sigma_3,\sigma_4=\pm\frac{1}{2}} 2 \text{Re} \{ \mathcal{M}_1^{\sigma_1,\sigma_2,\sigma_3,\sigma_4} (\mathcal{M}_0^{\sigma_1,\sigma_2,\sigma_3,\sigma_4})^* \}. \quad (3.5)$$

The actual calculation of the one-loop diagrams has been carried out in the 't Hooft–Feynman gauge. The Feynman graphs are evaluated in two completely independent ways, leading to two independent computer codes. The results of the two codes are in good numerical agreement (i.e. within more than 10 digits for non-exceptional phase-space points).

In the first calculation, the Feynman graphs are generated with *FeynArts* version 1.0 [38]. With the help of *Mathematica* routines the amplitudes are expressed in terms of SME and coefficients of tensor integrals. The output is processed into a *Fortran* program for the numerical evaluation. This calculation of the virtual corrections has been repeated using the background-field method [35], where the individual contributions from self-energy, vertex, and box corrections differ from their counterparts in the conventional formalism. The total one-loop corrections of the conventional and of the background-field approach were found to be in perfect numerical agreement.

The second calculation has been made using *FeynArts* version 3 [39] for the generation and *FormCalc* [40] for the evaluation of the amplitudes. The analytical results of *FormCalc* in terms of Weyl-spinor chains and their coefficients have been translated to *C++* code for the numerical evaluation.

### 3.2.2 Gauge-boson resonances and complex-mass scheme

The description of resonances in (standard) perturbation theory requires a Dyson summation of self-energy insertions in the resonant propagator in order to introduce the imaginary part provided by the finite decay width into the propagator denominator. This procedure in general violates gauge invariance, i.e. destroys Slavnov–Taylor or Ward identities and disturbs the cancellation of gauge-parameter dependences, because different perturbative orders are mixed (see, for instance, Ref. [41] and references therein).

In both of our two calculations we employ the so-called “complex-mass scheme”, which was introduced in Ref. [29] for lowest-order calculations and generalized to the one-loop level in Ref. [28]. In this approach the W- and Z-boson masses are consistently considered as complex quantities, defined as the locations of the propagator poles in the complex plane. To this end, bare real masses are split into complex renormalized masses and complex counterterms. Since the bare Lagrangian is not changed, double counting

does not occur. Perturbative calculations can be performed as usual, only parameters and counterterms, in particular the electroweak mixing angle defined from the ratio of the W- and Z-boson masses, become complex. Since we only perform an analytic continuation of the parameters, all relations that follow from gauge invariance, such as Ward identities, remain valid. As a consequence the amplitudes are gauge independent, and unitarity cancellations are respected. Moreover, the on-shell renormalization scheme can straightforwardly be transferred to the complex-mass scheme [28].

The use of complex gauge-boson masses necessitates the consistent use of these complex masses also in loop integrals. The scalar master integrals are evaluated for complex masses using the methods and results of Refs. [42, 43, 44].

We also treat the width of the top quark in the complex-mass scheme, i.e. we introduce a complex top-quark mass  $\mu_t$  via  $\mu_t^2 = m_t^2 - im_t\Gamma_t$ .

### 3.2.3 Numerically stable evaluation of one-loop integrals

The one-loop calculation of the decay  $H \rightarrow 4f$  requires the evaluation of 5-point one-loop tensor integrals. We calculate the 5-point integrals by directly reducing them to five 4-point functions, as described in Refs. [30, 31]. Note that this reduction does not involve inverse Gram determinants composed of external momenta, which naturally occur in the Passarino–Veltman reduction [45] of tensor to scalar integrals. The latter procedure leads to serious numerical problems when the Gram determinants become small.

Tensor 4-point and 3-point integrals are reduced to scalar integrals with the Passarino–Veltman algorithm [45] as long as no small Gram determinant appears in the reduction. If small Gram determinants occur, two alternative schemes are applied [31]. In one method, we evaluate a specific tensor coefficient, the integrand of which is logarithmic in Feynman parametrization, by numerical integration. Then the remaining coefficients as well as the standard scalar integral are algebraically derived from this coefficient. This method is used in the first loop calculation described in Section 3.2.1. The second, alternative method, which is used in the second loop calculation described in Section 3.2.1, makes use of expansions of the tensor coefficients about the limit of vanishing Gram determinants and possibly other kinematical determinants. In this way, all tensor coefficients can be expressed in terms of the standard scalar functions.

The whole procedure for the evaluation of the scalar and tensor one-loop integrals has been taken over from the one-loop calculation of  $e^+e^- \rightarrow 4$  fermions [28].

### 3.2.4 Input-parameter scheme

We use the “ $G_\mu$  scheme”, where a large universal part of the  $\mathcal{O}(\alpha)$  corrections is absorbed into the lowest-order prediction. In this scheme the electromagnetic coupling constant  $\alpha = e^2/(4\pi)$  is derived from the Fermi constant  $G_\mu$ , the muon decay constant, according to

$$\alpha_{G_\mu} = \frac{\sqrt{2}G_\mu M_W^2}{\pi} \left(1 - \frac{M_W^2}{M_Z^2}\right). \quad (3.6)$$

This procedure takes into account the running of the electromagnetic coupling constant  $\alpha(Q^2)$  from  $Q^2 = 0$  to the electroweak scale and also accounts for universal corrections related to the  $\rho$  parameter in the coupling of the W boson to fermions.

In order to avoid double-counting, the corrections absorbed in the lowest-order prediction by the use of  $\alpha_{G_\mu}$  have to be subtracted from the explicit  $\mathcal{O}(\alpha)$  corrections. To this end, we subtract the weak corrections to muon decay  $\Delta r$  [34, 46] from the corrections in the  $\alpha(0)$  (on-shell) scheme. This can be done by redefining the charge renormalization constant as

$$\delta Z_e|_{G_\mu} = \delta Z_e|_{\alpha(0)} - \frac{1}{2}(\Delta r)_{1\text{-loop}}, \quad (3.7)$$

where  $(\Delta r)_{1\text{-loop}}$  is the one-loop expression for  $\Delta r$  evaluated in the complex-mass scheme.

### 3.3 Leading two-loop corrections

Since corrections due to the self-interaction of the Higgs boson become important for large Higgs masses, we have included the dominant two-loop corrections to the decay  $H \rightarrow VV$  in the large-Higgs-mass limit which were calculated in Refs. [22, 23]. They are of order  $\mathcal{O}(G_\mu^2 M_H^4)$  and read

$$\int d\Gamma_{G_\mu^2 M_H^4} = 62.0308(86) \left( \frac{G_\mu M_H^2}{16\pi^2 \sqrt{2}} \right)^2 \int d\Gamma_0, \quad (3.8)$$

where the numerical prefactor has been taken from Ref. [23]. The error of this factor is far beyond other uncertainties and, thus, ignored in the numerics.

We do not include any higher-order corrections proportional to a power of  $G_\mu m_t^2$  since we already see at the one-loop level that the heavy-top limit does not provide a sound approximation of the corrections from closed fermion loops. In particular, for Higgs masses near and above the  $t\bar{t}$  threshold,  $M_H \gtrsim 2m_t$  the large- $m_t$  limit is not appropriate.

## 4 Real photon corrections

### 4.1 Matrix element for $H \rightarrow 4f\gamma$

The real photon corrections are induced by the process

$$H(p) \longrightarrow f_1(k_1, \sigma_1) + \bar{f}_2(k_2, \sigma_2) + f_3(k_3, \sigma_3) + \bar{f}_4(k_4, \sigma_4) + \gamma(k, \lambda), \quad (4.1)$$

where the momenta and helicities of the external particles are indicated in parentheses.

As for the lowest-order process, we consistently neglect fermion masses. However, we restore the mass-singular logarithms appearing in collinear photon emission as described in Section 4.2.

The matrix elements for the radiative process can be constructed in the same way as for the lowest-order process (2.1) from the set of generic diagrams that is obtained from Figure 1 by adding a photon line in all possible ways to the charged particles (including possible new graphs involving would-be Goldstone-boson exchange).

We have evaluated the generic helicity matrix elements  $\mathcal{M}_\gamma^{\sigma_a \sigma_b \sigma_c \sigma_d \lambda}(k_a, k_b, k_c, k_d, k)$  of this process again using the WvdW spinor technique in the formulation of Ref. [36]. The amplitudes generically read

$$\begin{aligned} \mathcal{M}_\gamma^{VV, \sigma_a \sigma_b \sigma_c \sigma_d \lambda}(Q_a, Q_b, Q_c, Q_d, k_a, k_b, k_c, k_d, k) = \\ 2\sqrt{2}e^4 g_{Vf_a f_b}^{\sigma_a} g_{Vf_c f_d}^{\sigma_c} g_{HVV} \delta_{\sigma_a, -\sigma_b} \delta_{\sigma_c, -\sigma_d} A_{\sigma_a \sigma_c \lambda}^{VV}(Q_a, Q_b, Q_c, Q_d, k_a, k_b, k_c, k_d, k), \end{aligned} \quad (4.2)$$

or more specifically for the case of Z-mediated and W-mediated decays

$$\begin{aligned}
\mathcal{M}_\gamma^{ZZ, \sigma_a \sigma_b \sigma_c \sigma_d \lambda}(Q_a, Q_b, Q_c, Q_d, k_a, k_b, k_c, k_d, k) = \\
\frac{2\sqrt{2}e^4 g_{Zf_a f_b}^{\sigma_a} g_{Zf_c f_d}^{\sigma_c} \mu_W}{c_W^2 s_W} \delta_{\sigma_a, -\sigma_b} \delta_{\sigma_c, -\sigma_d} A_{\sigma_a \sigma_c \lambda}^{ZZ}(Q_a, Q_b, Q_c, Q_d, k_a, k_b, k_c, k_d, k), \\
\mathcal{M}_\gamma^{WW, \sigma_a \sigma_b \sigma_c \sigma_d \lambda}(Q_a, Q_b, Q_c, Q_d, k_a, k_b, k_c, k_d, k) = \\
\frac{\sqrt{2}e^4 \mu_W}{s_W^3} \delta_{\sigma_a, -\sigma_b, +} \delta_{\sigma_c, -\sigma_d, +} A_{--\lambda}^{WW}(Q_a, Q_b, Q_c, Q_d, k_a, k_b, k_c, k_d, k). \tag{4.3}
\end{aligned}$$

The auxiliary functions are given by

$$\begin{aligned}
A_{---}^{VV}(Q_a, Q_b, Q_c, Q_d, k_a, k_b, k_c, k_d, k) = \\
\langle k_b k_d \rangle^* \left[ \frac{\langle k_a k_b \rangle^* \langle k_a k_c \rangle + \langle k k_b \rangle^* \langle k k_c \rangle}{[(k_a + k_b + k)^2 - \mu_V^2][(k_c + k_d)^2 - \mu_V^2]} \right. \\
\times \left( \frac{Q_a}{\langle k k_a \rangle^* \langle k k_b \rangle^*} + \frac{Q_a - Q_b}{(k_a + k_b)^2 - \mu_V^2} \frac{\langle k k_a \rangle}{\langle k k_b \rangle^*} \right) \\
- \frac{\langle k_c k_d \rangle^* \langle k_c k_a \rangle + \langle k k_d \rangle^* \langle k k_a \rangle}{[(k_a + k_b)^2 - \mu_V^2][(k_c + k_d + k)^2 - \mu_V^2]} \\
\times \left( \frac{Q_c}{\langle k k_c \rangle^* \langle k k_d \rangle^*} + \frac{Q_c - Q_d}{(k_c + k_d)^2 - \mu_V^2} \frac{\langle k k_c \rangle}{\langle k k_d \rangle^*} \right) \\
\left. + \frac{Q_a - Q_b}{[(k_a + k_b)^2 - \mu_V^2][(k_c + k_d)^2 - \mu_V^2]} \frac{\langle k_b k_d \rangle^* \langle k_a k_c \rangle}{\langle k k_b \rangle^* \langle k k_d \rangle^*} \right], \\
A_{+--}^{VV}(Q_a, Q_b, Q_c, Q_d, k_a, k_b, k_c, k_d, k) = A_{---}^{VV}(-Q_b, -Q_a, Q_c, Q_d, k_b, k_a, k_c, k_d, k), \\
A_{-+-}^{VV}(Q_a, Q_b, Q_c, Q_d, k_a, k_b, k_c, k_d, k) = A_{---}^{VV}(Q_a, Q_b, -Q_d, -Q_c, k_a, k_b, k_d, k_c, k), \\
A_{++-}^{VV}(Q_a, Q_b, Q_c, Q_d, k_a, k_b, k_c, k_d, k) = A_{---}^{VV}(-Q_b, -Q_a, -Q_d, -Q_c, k_b, k_a, k_d, k_c, k), \\
A_{\sigma_a \sigma_c +}^{VV}(Q_a, Q_b, Q_c, Q_d, k_a, k_b, k_c, k_d, k) = \\
\left( A_{-\sigma_a, -\sigma_c, -}^{VV}(Q_a, Q_b, Q_c, Q_d, k_a, k_b, k_c, k_d, k) \right)^* \Big|_{\mu_V \rightarrow \mu_V^*}, \tag{4.4}
\end{aligned}$$

and obey the relations

$$\begin{aligned}
A_{-\sigma_a, -\sigma_c, -\lambda}^{VV}(Q_a, Q_b, Q_c, Q_d, k_a, k_b, k_c, k_d, k) = \\
\left( A_{\sigma_a \sigma_c \lambda}^{VV}(Q_a, Q_b, Q_c, Q_d, k_a, k_b, k_c, k_d, k) \right)^* \Big|_{\mu_V \rightarrow \mu_V^*}, \\
A_{-\sigma_a, \sigma_c, \lambda}^{VV}(Q_a, Q_b, Q_c, Q_d, k_a, k_b, k_c, k_d, k) = \\
A_{\sigma_a \sigma_c \lambda}^{VV}(-Q_b, -Q_a, Q_c, Q_d, k_b, k_a, k_c, k_d, k), \\
A_{\sigma_a, -\sigma_c, \lambda}^{VV}(Q_a, Q_b, Q_c, Q_d, k_a, k_b, k_c, k_d, k) = \\
A_{\sigma_a \sigma_c \lambda}^{VV}(Q_a, Q_b, -Q_d, -Q_c, k_a, k_b, k_d, k_c, k), \\
A_{\sigma_a, \sigma_c, -\lambda}^{VV}(Q_a, Q_b, Q_c, Q_d, k_a, k_b, k_c, k_d, k) = \\
-\left( A_{\sigma_c \sigma_a \lambda}^{VV}(Q_d, Q_c, Q_b, Q_a, k_d, k_c, k_b, k_a, k) \right)^* \Big|_{\mu_V \rightarrow \mu_V^*}, \\
A_{\sigma_a \sigma_c \lambda}^{VV}(Q_a, Q_b, Q_c, Q_d, k_a, k_b, k_c, k_d, k) = \\
A_{\sigma_c \sigma_a \lambda}^{VV}(Q_c, Q_d, Q_a, Q_b, k_c, k_d, k_a, k_b, k). \tag{4.5}
\end{aligned}$$

The relations between the  $A_{\dots}$  functions that differ in all helicities result from a P transformation. Those, where only one fermion helicity is reversed are related to C symmetry. The last but one is due to CP symmetry, and the last one results from a symmetry under the exchange of the two fermion pairs. The charges of the fermions are related by

$$Q_a - Q_b + Q_c - Q_d = 0. \quad (4.6)$$

For the Z-mediated decays, where  $Q_a = Q_b$  and  $Q_c = Q_d$ , the auxiliary function (4.4) simplifies to

$$\begin{aligned} A_{---}^{ZZ}(Q_a, Q_a, Q_c, Q_c, k_a, k_b, k_c, k_d, k) = \\ \langle k_b k_d \rangle^* \left[ \frac{\langle k_a k_b \rangle^* \langle k_a k_c \rangle + \langle k k_b \rangle^* \langle k k_c \rangle}{[(k_a + k_b + k)^2 - \mu_V^2][(k_c + k_d)^2 - \mu_V^2]} \frac{Q_a}{\langle k k_a \rangle^* \langle k k_b \rangle^*} \right. \\ \left. - \frac{\langle k_c k_d \rangle^* \langle k_c k_a \rangle + \langle k k_d \rangle^* \langle k k_a \rangle}{[(k_a + k_b)^2 - \mu_V^2][(k_c + k_d + k)^2 - \mu_V^2]} \frac{Q_c}{\langle k k_c \rangle^* \langle k k_d \rangle^*} \right]. \end{aligned} \quad (4.7)$$

From the generic matrix element  $\mathcal{M}_\gamma^{VV, \sigma_a \sigma_b \sigma_c \sigma_d \lambda}(k_a, k_b, k_c, k_d, k)$  the matrix elements for the specific processes can be constructed in complete analogy to the process without photon as in (2.11)–(2.14).

The squares of the matrix elements (4.2) have been successfully checked against the result obtained with the package MADGRAPH [47] numerically.

The contribution  $\Gamma_\gamma$  of the radiative decay to the total decay width is given by

$$\int d\Gamma_\gamma = \frac{1}{2M_H} \int d\Phi_\gamma \sum_{\sigma_1, \sigma_2, \sigma_3, \sigma_4 = \pm \frac{1}{2}} \sum_{\lambda = \pm 1} |\mathcal{M}_\gamma^{\sigma_1 \sigma_2 \sigma_3 \sigma_4 \lambda}|^2, \quad (4.8)$$

where the phase-space integral is defined by

$$\int d\Phi_\gamma = \int \frac{d^3 \mathbf{k}}{(2\pi)^3 2k^0} \left( \prod_{i=1}^4 \int \frac{d^3 \mathbf{k}_i}{(2\pi)^3 2k_i^0} \right) (2\pi)^4 \delta^{(4)} \left( p - k - \sum_{j=1}^4 k_j \right). \quad (4.9)$$

Without introducing soft and collinear regulators this phase-space integral diverges in the soft ( $k^0 \rightarrow 0$ ) and collinear ( $k k_i \rightarrow 0$ ) regions. The applied solutions are outlined in the next section.

## 4.2 Treatment of soft and collinear divergences

In the combination of virtual and real photon corrections, the fermion-mass effects have to be restored in the phase-space regions of collinear photon radiation off charged fermions, and the IR regularization for soft-photon emission has to be implemented. To this end, we employ the dipole subtraction formalism for photon radiation [32] as well as the more conventional phase-space slicing approach.

The actual calculation exactly follows the one described in Ref. [33], where electroweak corrections to the related process  $\gamma\gamma \rightarrow WW \rightarrow 4f$  have been calculated. The structure of soft and collinear singularities of this process is exactly the same as in the decay  $H \rightarrow 4f$  considered in this work, because both processes involve the same pattern

of charged particles in the initial and final states. Consequently, apart from obvious substitutions for the flux factors all formulas given in Section 4 of Ref. [33] for cross sections literally carry over to our decay widths.

In the matching of real and virtual corrections the issue of collinear safety of observables is crucial. We speak of collinear-safe observables if a nearly collinear system of a charged fermion and a photon is treated inclusively, i.e. if phase-space selection cuts (or histogram bins of distributions) depend only on the sum  $k_i + k$  of the nearly collinear fermion and photon momenta. In this case the energy fraction

$$z_i = \frac{k_i^0}{k_i^0 + k^0} \quad (4.10)$$

of a charged fermion  $f_i$  after emitting a photon in a sufficiently small cone around its direction of flight is fully integrated over, because it is not constrained by any phase-space cut (or histogram bin selection in distributions). Thus, the Kinoshita–Lee–Nauenberg (KLN) theorem [48] guarantees that all singularities connected with FSR cancel between the virtual and real corrections, even though they are defined on different phase spaces. The full phase-space integration in  $H \rightarrow 4f(+\gamma)$ , which leads to partial decay widths, is trivially collinear safe. More generally, a sufficient inclusiveness is achieved by the photon recombination described in Section 7.1, which treats outgoing charged fermions and photons as one quasi-particle if they are very close in angle. The original version of the dipole subtraction formalism for photon radiation [32] deals with collinear-safe situations only. The generalization to the non-collinear-safe FSR is described in Ref. [33].

Figures 5 and 6 illustrate the agreement between the subtraction and slicing methods for the partial decay widths of the two decay channels  $H \rightarrow \nu_e e^+ \mu^- \bar{\nu}_\mu$  and  $H \rightarrow e^- e^+ \mu^- \mu^+$ . These results were obtained with  $5 \cdot 10^7$  events. In the slicing approach, the phase-space regions of soft or collinear photons are defined by the auxiliary cutoff parameters  $\Delta E \ll \Gamma_W$  and  $\Delta\theta \ll 1$ . The region  $k^0 < \Delta E$  is treated in soft-photon approximation, the regions  $\theta_{\gamma f} < \Delta\theta$ ,  $k^0 > \Delta E$  ( $\theta_{\gamma f}$  is the emission angle from any fermion  $f$ ) are evaluated using collinear factorization. In the remaining regular phase space no regulators (photon and fermion masses) are used. Therefore, the slicing result is correct up to terms of  $\mathcal{O}(\Delta E)$  and  $\mathcal{O}(\Delta\theta)$ . For decreasing auxiliary parameters  $\Delta E$  and  $\Delta\theta$ , the slicing result reaches a plateau, as it should be, until the increasing statistical errors become large and eventually underestimated. In the plateau region the slicing and subtraction results are compatible within statistical errors, but the subtraction result shows smaller integration errors although the same number of events is used.

### 4.3 Higher-order final-state radiation

Photons that are emitted collinear off a charged fermion give rise to corrections that are enhanced by large logarithms of the form  $\alpha \log m_f^2/M^2$ , where  $m_f$  is a fermion mass and  $M$  is some typical energy scale. If the photons are treated fully inclusively, as it is the case if the photons are recombined with the corresponding fermion, these logarithms cancel due to the KLN theorem [48]. If, however, distributions like in the invariant mass of two fermions, as discussed in Section 7, are to be considered without recombining collinear photons, then these logarithms do not cancel and yield large effects. Thus, corrections of this origin should be taken into account beyond  $\mathcal{O}(\alpha)$ . This can be achieved

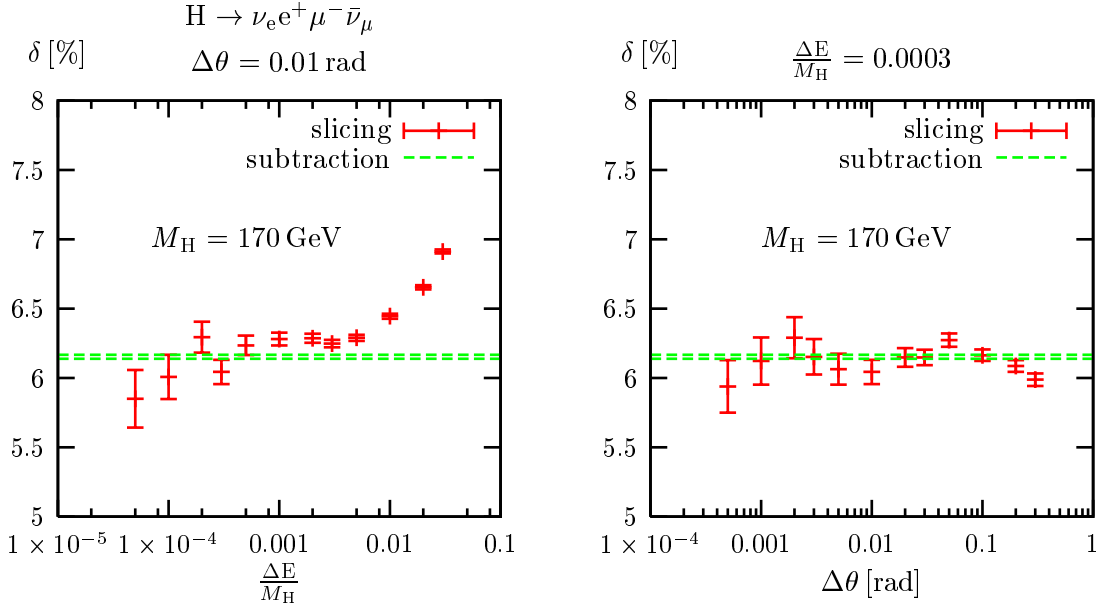


Figure 5: Dependence of the relative corrections  $\delta$  to the partial decay width on the energy cutoff  $\Delta E$  (l.h.s.) and on the angular cutoff  $\Delta\theta$  (r.h.s.) in the slicing approach for the decay  $H \rightarrow \nu_e e^+ \mu^- \bar{\nu}_\mu$  with  $M_H = 170$  GeV. For comparison the corresponding result obtained with the dipole subtraction method is shown as a  $1\sigma$  band in the plots.

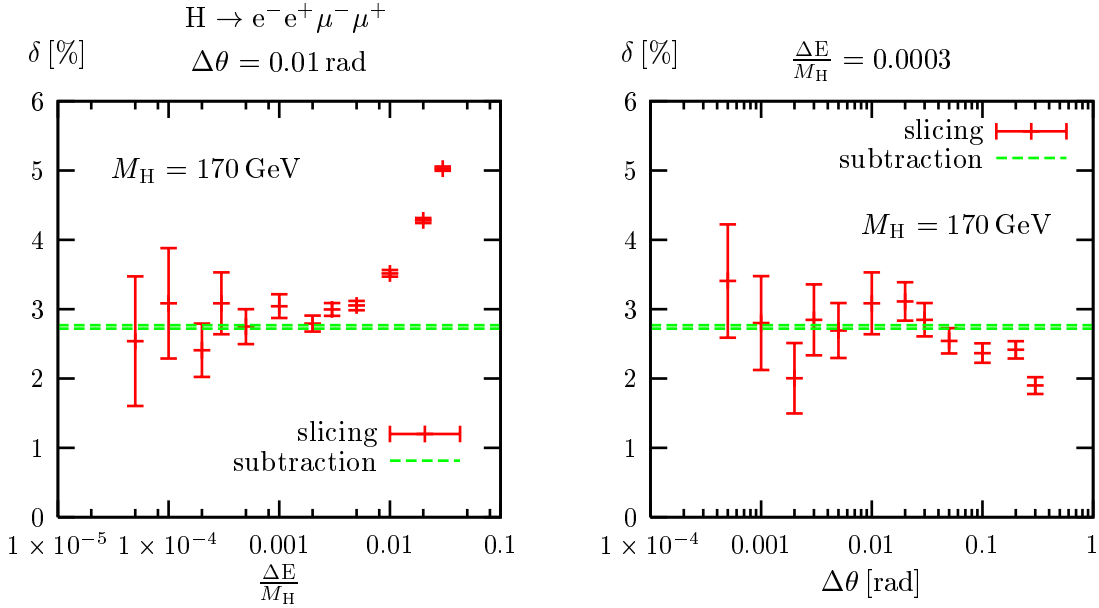


Figure 6: Same as in Figure 5 but for the decay  $H \rightarrow e^- e^+ \mu^- \mu^+$ .



in the structure-function approach [ 49] which is based on the mass-factorization theorem. According to this theorem the decay width including the leading-logarithmic FSR terms can be written as

$$\int d\Gamma_{\text{LLFSR}} = \prod_{\substack{i=1 \\ Q_i \neq 0}}^4 \left[ \int_0^1 dz_i \Gamma_{ii}^{\text{LL}}(z_i, M^2) \right] \int d\Gamma_0 \Theta_{\text{cut}}(\{z_j k_j\}). \quad (4.11)$$

The function  $\Theta_{\text{cut}}(\{z_j k_j\})$  generically denotes all histogram routines or phase-space cuts. It depends on the fermion momenta  $z_j k_j$  which, in the case of charged fermions, may be reduced by the factor  $z_j$  due to collinear photon emission. For neutral fermions we have  $z_j = 1$ . The structure functions including terms up to  $\mathcal{O}(\alpha^3)$ , improved by the exponentiation of the soft-photon parts, read [ 50]

$$\begin{aligned} \Gamma_{ii}^{\text{LL,exp}}(z, M^2) = & \frac{\exp\left(-\frac{1}{2}\beta_i \gamma_E + \frac{3}{8}\beta_i\right)}{\Gamma\left(1 + \frac{1}{2}\beta_i\right)} \frac{\beta_i}{2} (1-z)^{\frac{\beta_i}{2}-1} - \frac{\beta_i}{4} (1+z) \\ & - \frac{\beta_i^2}{32} \left\{ \frac{1+3z^2}{1-z} \ln(z) + 4(1+z) \ln(1-z) + 5 + z \right\} \\ & - \frac{\beta_i^3}{384} \left\{ (1+z) \left[ 6 \text{Li}_2(z) + 12 \ln^2(1-z) - 3\pi^2 \right] \right. \\ & \quad + \frac{1}{1-z} \left[ \frac{3}{2} (1+8z+3z^2) \ln(z) + 6(z+5)(1-z) \ln(1-z) \right. \\ & \quad \quad + 12(1+z^2) \ln(z) \ln(1-z) - \frac{1}{2} (1+7z^2) \ln^2(z) \\ & \quad \quad \left. \left. + \frac{1}{4} (39 - 24z - 15z^2) \right] \right\} \end{aligned} \quad (4.12)$$

with  $\gamma_E$  and  $\Gamma(y)$  denoting Euler's constant and the Gamma function, respectively. The mass-singular logarithm

$$\beta_i = \frac{2Q_i^2 \alpha(0)}{\pi} \left[ \ln\left(\frac{M^2}{m_i^2}\right) - 1 \right] \quad (4.13)$$

involves a scale  $M$ , which is not fixed in leading logarithmic order and should be set to a scale typical for the process under consideration. We use  $M^2 = M_H^2$  in our evaluations. The appropriate coupling in the leading-logarithmic terms is  $\alpha(0)$ , since these originate from real or virtual soft or collinear photons. As the function  $(1-z)^{\frac{\beta_i}{2}-1}$  is difficult to integrate numerically, an appropriate mapping has to be chosen.

In order to study the influence of the higher-order terms we alternatively expand the exponential up to terms of  $\mathcal{O}(\alpha^3)$ , yielding

$$\begin{aligned} \Gamma_{ii}^{\text{LL}}(z, M^2) = & \delta(1-z) + \left[ \frac{\beta_i}{4} \frac{1+z^2}{1-z} \right. \\ & + \frac{\beta_i^2}{32} \left\{ \frac{1+4z+z^2}{1-z} - \frac{1+3z^2}{1-z} \ln(z) + 4 \frac{1+z^2}{1-z} \ln(1-z) \right\} \\ & \left. + \frac{\beta_i^3}{1536} \left\{ \frac{15+24z+15z^2}{1-z} - 4\pi^2 \frac{1+3z^2}{1-z} - 6 \frac{1+8z+3z^2}{1-z} \ln(z) \right\} \right] \end{aligned}$$

$$\begin{aligned}
& + 24 \frac{1+4z+z^2}{1-z} \ln(1-z) - 24(1+z) \text{Li}_2(z) + 48 \frac{1+z^2}{1-z} \ln^2(1-z) \\
& - 48 \frac{1+z^2}{1-z} \ln(z) \ln(1-z) + 2 \frac{1+7z^2}{1-z} \ln^2(z) \Big\} \Big]_+, \tag{4.14}
\end{aligned}$$

where the  $[\dots]_+$  prescription is defined as usual,

$$\int_0^1 dz [f(z)]_+ g(z) \equiv \int_0^1 dz f(z) [g(z) - g(1)], \tag{4.15}$$

We convolute the lowest-order width according to (4.11) and add this to the result for the  $\mathcal{O}(\alpha)$ -corrected width. In order to avoid double counting, we have to subtract

$$\int d\Gamma_{\text{LLFSR},1} = \int d\Gamma_0 + \int d\Gamma_0 \sum_{\substack{i=1 \\ Q_i \neq 0}}^4 \left[ \int_0^1 dz_i \Gamma_{ii}^{\text{LL},1}(z_i, M^2) \Theta_{\text{cut}}(z_i k_i, \{k_{j \neq i}\}) \right], \tag{4.16}$$

i.e. the leading logarithmic terms up to  $\mathcal{O}(\alpha)$ , from  $\int d\Gamma_{\text{LLFSR}}$ . They are defined by

$$\Gamma_{ii}^{\text{LL},1}(z, M^2) = \frac{\beta_{i,G_\mu}}{4} \left( \frac{1+z^2}{1-z} \right)_+. \tag{4.17}$$

Note that we have to subtract the  $\mathcal{O}(\alpha)$  terms according to the scheme that is applied for the virtual corrections. Since we work in the  $G_\mu$  scheme,  $\beta_{i,G_\mu}$  is proportional to  $\alpha_{G_\mu}$ , as defined in Section 7.

## 5 Final prediction and Monte Carlo integration

Summarizing all contributions to the differential decay width, (2.17), (3.5), (3.8), (4.8), (4.11), and (4.16), we get the following prediction,

$$\int d\Gamma = \int d\Gamma_0 + \int d\Gamma_{\text{virt}} + \int d\Gamma_{G_\mu^2 M_H^4} + \int d\Gamma_\gamma + \int d\Gamma_{\text{LLFSR}} - \int d\Gamma_{\text{LLFSR},1}. \tag{5.1}$$

The phase-space integrations are performed using the multi-channel Monte Carlo technique [51] where the integrand is flattened by choosing appropriate mappings of the pseudo-random numbers into the momenta of the outgoing particles. In more detail, the Monte Carlo part of PROPHECY4F builds upon the existing generators RACOONWW [29, 52] and COFFER $\gamma\gamma$  [33, 53]. The results obtained with the multi-channel technique have been checked against a second integration program based on the adaptive integration program VEGAS [54]. Although VEGAS already performs some adaption to the integrand structure a further improvement of the numerical error has been achieved by using mappings of the integration variables designed to flatten the resonances.

The numerical results presented below have been obtained using  $5 \cdot 10^7$  events except for the plots showing the decay width as a function of the Higgs mass which were calculated using  $2 \cdot 10^7$  events per point. Since the virtual corrections (rendered finite by adding the soft and collinear singularities from the real corrections), and also their statistical error, are at least a factor 10 smaller than the lowest-order values for moderate Higgs masses, we only evaluated the virtual corrections every 100th time, which improves the run-time of the program but does not deteriorate the overall statistical error. Soft and collinear singularities were treated with the subtraction method in the results shown below.

## 6 Improved-Born Approximation

The electroweak corrections contain large contributions of universal origin. Besides final-state radiation, which is discussed in Section 4.3, these consist, in particular, of the corrections associated with the running of  $\alpha$ , corrections proportional to  $m_t^2/M_W^2$ , and corrections proportional to  $M_H^2/M_W^2$ . By suitable parametrization of the lowest-order matrix elements, some of these universal corrections can be incorporated in the lowest order, thus reducing the remaining corrections. This does not only reduce the  $\mathcal{O}(\alpha)$  corrections but in general also the higher-order corrections. Corrections associated with the running of  $\alpha$ , and corrections related to the  $\rho$  parameter in the W-boson–fermion coupling are incorporated in the lowest-order prediction by using the  $G_\mu$  scheme.

Some loop diagrams involving top quarks lead to corrections that are enhanced by a large coupling factor  $G_\mu m_t^2$  in the limit of a large top-quark mass  $m_t$ . For the HZZ and HWW vertices this type of corrections was considered even up to two-loop order in Ref. [21]. However, the pure heavy-top limit  $m_t \rightarrow \infty$  is only applicable for  $M_H \ll 2m_t$ . Since we are also interested in  $M_H$  values near and above the  $t\bar{t}$  threshold, we instead consider the more general limit  $m_t, M_H \gg M_W, M_Z, m_{f \neq t}$ , i.e. we do not assume any hierarchy between the Higgs and the top-quark masses. We evaluate all closed fermion loops in this limit and keep only contributions that are enhanced by  $m_t^2$  times any function of the ratio  $M_H/m_t$ . The numerical analysis shows that this procedure yields a very good approximation for the sum of all closed fermion loops in the  $G_\mu$  scheme. In order to approximate the remaining bosonic corrections, the leading one- and two-loop corrections to the HVV vertices in the large-Higgs-mass limit, which are proportional to  $G_\mu M_H^2$  and  $G_\mu^2 M_H^4$ , respectively, are included in the IBA; these corrections are taken from Refs. [22, 23]. Moreover, for  $H \rightarrow WW \rightarrow 4f$  we include the leading effect  $\delta_{\text{Coul}}$  of the Coulomb singularity as calculated in Ref. [55], which originates from soft-photon exchange between the two slowly moving W bosons near the WW threshold. Finally, we take into account the QCD corrections to the gauge-boson decays if quarks are involved in the final states. The remaining corrections are expected to be widely independent of Higgs mass  $M_H$  and of the choice of the  $4f$  final state.

Our IBA for the partial decay widths, which is constructed according to these lines, reads

$$\begin{aligned} \int d\Gamma_{\text{IBA}}^{H \rightarrow ZZ \rightarrow 4f} &= \frac{1}{2M_H} \int d\Phi_0 \sum_{\sigma_1, \sigma_2, \sigma_3, \sigma_4 = \pm} |\mathcal{M}_0^{ZZ, \sigma_1 \sigma_2 \sigma_3 \sigma_4}|^2 \\ &\quad \times \text{Re} \left\{ 1 + \frac{G_\mu \mu_t^2}{8\sqrt{2}\pi^2} \left[ 1 - \frac{6c_W}{s_W} \left( \frac{Q_{f_1}}{g_{Zf_1f_1}^{\sigma_1}^2} + \frac{Q_{f_3}}{g_{Zf_3f_3}^{\sigma_3}^2} \right) + \tau_{\text{HZZ}} \left( \frac{M_H^2}{\mu_t^2} \right) \right] \right. \\ &\quad + \frac{G_\mu M_H^2}{8\sqrt{2}\pi^2} \left( \frac{5\pi^2}{6} - 3\sqrt{3}\pi + \frac{19}{2} \right) + 62.0308(86) \left( \frac{G_\mu M_H^2}{16\pi^2 \sqrt{2}} \right)^2 \\ &\quad \left. + \delta_{Z \rightarrow f_1 \bar{f}_2}^{\text{QCD}} + \delta_{Z \rightarrow f_3 \bar{f}_4}^{\text{QCD}} + c_{\text{HZZ}} \right\}, \\ \int d\Gamma_{\text{IBA}}^{H \rightarrow WW \rightarrow 4f} &= \frac{1}{2M_H} \int d\Phi_0 |\mathcal{M}_0^{\text{WW}, -+-+}|^2 \end{aligned}$$

$$\begin{aligned}
& \times \text{Re} \left\{ 1 + \frac{G_\mu \mu_t^2}{8\pi^2 \sqrt{2}} \left[ -5 + \tau_{\text{HWW}} \left( \frac{M_{\text{H}}^2}{\mu_t^2} \right) \right] \right. \\
& + \frac{G_\mu M_{\text{H}}^2}{8\sqrt{2}\pi^2} \left( \frac{5\pi^2}{6} - 3\sqrt{3}\pi + \frac{19}{2} \right) + 62.0308(86) \left( \frac{G_\mu M_{\text{H}}^2}{16\pi^2 \sqrt{2}} \right)^2 \\
& + g(\bar{\beta}) \delta_{\text{Coul}} \left( M_{\text{H}}^2, (k_1 + k_2)^2, (k_3 + k_4)^2 \right) \\
& \left. + \delta_{\text{W} \rightarrow f_1 \bar{f}_2}^{\text{QCD}} + \delta_{\text{W} \rightarrow f_3 \bar{f}_4}^{\text{QCD}} + c_{\text{HWW}} \right\}, \tag{6.1}
\end{aligned}$$

where the terms proportional to a charge factor  $Q_f$  are absent if  $f$  is a neutrino. The phase-space integral was defined in (2.18). The auxiliary functions  $\tau_{\text{HVV}}$ , which appear in (6.1), are given by

$$\begin{aligned}
\tau_{\text{HZZ}} \left( \frac{M_{\text{H}}^2}{\mu_t^2} \right) &= 20 + 6\beta_t^2 + 3\beta_t(\beta_t^2 + 1) \ln(x_t) + 3(1 - \beta_t^2) \ln^2(x_t), \\
\tau_{\text{HWW}} \left( \frac{M_{\text{H}}^2}{\mu_t^2} \right) &= 8 + 12\beta_t^2 + 3\beta_t(3\beta_t^2 - 1) \ln(x_t) + \frac{3}{2}(1 - \beta_t^2)^2 \ln^2(x_t), \tag{6.2}
\end{aligned}$$

where

$$\beta_t = \sqrt{1 - \frac{4\mu_t^2}{M_{\text{H}}^2}}, \quad x_t = \frac{\beta_t - 1}{\beta_t + 1}. \tag{6.3}$$

They have the property  $\tau_{\text{HVV}}(0) = 0$ , i.e. they quantify the deviation of the  $m_t^2/M_{\text{W}}^2$ -enhanced corrections from the pure heavy-top limit, which are made explicit in (6.1). Note that we consistently use the complex top mass  $\mu_t$  instead of  $m_t$ . The correction factor  $\delta_{\text{Coul}}$  containing the Coulomb singularity reads [55]

$$\begin{aligned}
\delta_{\text{Coul}}(s, k_+^2, k_-^2) &= \frac{\alpha(0)}{\bar{\beta}} \text{Im} \left\{ \ln \left( \frac{\beta - \bar{\beta} + \Delta_M}{\beta + \bar{\beta} + \Delta_M} \right) \right\}, \\
\bar{\beta} &= \frac{\sqrt{s^2 + k_+^4 + k_-^4 - 2sk_+^2 - 2sk_-^2 - 2k_+^2 k_-^2}}{s}, \\
\beta &= \sqrt{1 - \frac{4\mu_{\text{W}}^2}{s}}, \quad \Delta_M = \frac{|k_+^2 - k_-^2|}{s}, \tag{6.4}
\end{aligned}$$

with the fine-structure constant  $\alpha(0)$ . The auxiliary function

$$g(\bar{\beta}) = (1 - \bar{\beta}^2)^2 \tag{6.5}$$

restricts the impact of  $\delta_{\text{Coul}}$  to the WW threshold region where it is valid. The QCD corrections  $\delta_{V \rightarrow f_i \bar{f}_j}^{\text{QCD}}$  to the gauge-boson decays are given by

$$\delta_{V \rightarrow l_i \bar{l}_j}^{\text{QCD}} = 0, \quad \delta_{V \rightarrow q_i \bar{q}_j}^{\text{QCD}} = \frac{\alpha_s}{\pi}, \tag{6.6}$$

according to whether  $f_i \bar{f}_j$  is a lepton ( $l_i \bar{l}_j$ ) or a quark ( $q_i \bar{q}_j$ ) pair, respectively. Finally, the “constants”  $c_{\text{HVV}}$  have been introduced to account for a sizeable, but widely  $M_{\text{H}}$ -independent offset in the relative corrections to the HVV vertices that is induced by

non-leading corrections. In practice, it is often sufficient to set  $c_{\text{HVV}}$  to a numerical constant, which can be determined from a comparison with the full correction to the  $\text{H} \rightarrow \text{VV} \rightarrow 4f$  process. For the input parameters given in Section 7.1 we find that the choice

$$c_{\text{HZZ}} = 3\%, \quad c_{\text{HWW}} = 4\% \quad (6.7)$$

is appropriate. The values of  $c_{\text{HVV}}$  will certainly not change significantly if the input parameters of Section 7.1 vary within their experimental uncertainties.

When defining the IBA for the final states  $f\bar{f}f\bar{f}$  and  $f\bar{f}f'\bar{f}'$  we make use of the fact that the two subamplitudes in (2.13) and (2.14) have a very small interference. Therefore, we define the IBA for the squared matrix element from the IBA of the corresponding squared subamplitudes and take into account the interference in lowest order without modification.

In deriving the contributions enhanced by  $m_t^2$  in (6.1), we used a double-pole approximation and implicitly assumed an integration over all decay angles. Without this assumption, corrections to angular correlations are induced by the interference of the two relevant formfactors describing the  $\text{HVV}$  vertices. Hence, the IBA (6.1) is in first place constructed for partial widths.

## 7 Numerical results

### 7.1 Input parameters and setup

We use the following set of input parameters [56],

$$\begin{aligned} G_\mu &= 1.16637 \times 10^{-5} \text{ GeV}^{-2}, & \alpha(0) &= 1/137.03599911, & \alpha_s &= 0.1187, \\ M_W^{\text{LEP}} &= 80.425 \text{ GeV}, & \Gamma_W^{\text{LEP}} &= 2.124 \text{ GeV}, \\ M_Z^{\text{LEP}} &= 91.1876 \text{ GeV}, & \Gamma_Z^{\text{LEP}} &= 2.4952 \text{ GeV}, \\ m_e &= 0.51099892 \text{ MeV}, & m_\mu &= 105.658369 \text{ MeV}, & m_\tau &= 1.77699 \text{ GeV}, \\ m_u &= 66 \text{ MeV}, & m_c &= 1.2 \text{ GeV}, & m_t &= 174.3 \text{ GeV}, \\ m_d &= 66 \text{ MeV}, & m_s &= 150 \text{ MeV}, & m_b &= 4.3 \text{ GeV}. \end{aligned} \quad (7.1)$$

The masses of the light quarks are adjusted to reproduce the hadronic contribution to the photonic vacuum polarization of Ref. [57]. As discussed in Section 3.2.4, we use the  $G_\mu$  scheme, i.e. we derive the electromagnetic coupling constant from the Fermi constant according to (3.6). We use  $\alpha_{G_\mu}$  everywhere except for the couplings of the collinear photons, as described in Section 4.3. In this case we use  $\alpha(0)$ , because this reflects the coupling behaviour of real photons.

Using the complex-mass scheme, we employ a fixed width in the resonant W- and Z-boson propagators in contrast to the approach used at LEP to fit the W and Z resonances, where running widths are taken. Therefore, we have to convert the “on-shell” values of  $M_V^{\text{LEP}}$  and  $\Gamma_V^{\text{LEP}}$  ( $V = \text{W}, \text{Z}$ ), resulting from LEP, to the “pole values” denoted by  $M_V$  and  $\Gamma_V$  in this paper. The relation between the two sets of values is given by [58]

$$M_V = M_V^{\text{LEP}} / \sqrt{1 + (\Gamma_V^{\text{LEP}} / M_V^{\text{LEP}})^2}, \quad \Gamma_V = \Gamma_V^{\text{LEP}} / \sqrt{1 + (\Gamma_V^{\text{LEP}} / M_V^{\text{LEP}})^2}, \quad (7.2)$$

leading to

$$M_W = 80.397 \text{ GeV}, \quad M_Z = 91.1535 \text{ GeV}. \quad (7.3)$$

We make use of these mass parameters in the numerics discussed below, although the difference between using  $M_V$  or  $M_V^{\text{LEP}}$  would be hardly visible. The widths of the gauge bosons W and Z,  $\Gamma_W$  and  $\Gamma_Z$ , are calculated from the above input including  $\mathcal{O}(\alpha)$  corrections, but using real mass parameters everywhere. Alternatively, the experimental widths calculated from (7.2) could be used, but the procedure pursued here ensures that the “effective branching ratios” of the W’s and Z’s, which result from the integration over their decays, add up to one if all decay channels are summed over. The gauge-boson widths depend on the Higgs mass only weakly. For the Higgs masses  $M_H = 140, 170, 200 \text{ GeV}$  the corresponding values are given in Table 1. These values are used everywhere in the complex masses, i.e. we also apply the  $\mathcal{O}(\alpha)$ -corrected W and Z widths for the lowest-order predictions.

In order to improve the corrections for partial Higgs decay widths for a Higgs mass near the  $t\bar{t}$  threshold ( $M_H \sim 2m_t$ ), we evaluate loop diagrams with internal top quarks with a complex top-quark mass  $\mu_t = \sqrt{m_t^2 - im_t\Gamma_t}$ . To this end, we set the top-quark width to its lowest-order prediction in the SM,

$$\Gamma_t = \frac{G_\mu(m_t^2 - M_W^2)^2(m_t^2 + 2M_W^2)}{8\pi\sqrt{2}m_t^3} = 1.54 \text{ GeV}, \quad (7.4)$$

where the simplifications  $m_b = 0$  and  $V_{tb} = 1$  are used.

The angular distributions in Section 7.5 are defined in the rest frame of the Higgs boson. All observables are calculated without applying phase-space cuts, and, if not stated otherwise, a photon recombination is performed. More precisely, if the invariant mass of a photon and a charged fermion is smaller than 5 GeV, the photon momentum is added to the fermion momentum in the histograms. If this condition applies to more than one fermion the photon is recombined with the fermion that yields the smallest invariant mass for the resulting fermion–photon pair.

All but the lowest-order predictions contain the higher-order FSR as described in Section 4.3 as well as the two-loop corrections proportional to  $G_\mu^2 M_H^4$  given in Section 3.3.

## 7.2 Results for partial decay widths

In Table 1 the partial decay width including  $\mathcal{O}(\alpha)$  corrections is shown for different decay channels and different values of the Higgs mass. In parentheses the statistical error of the phase-space integration is indicated, and  $\delta = \Gamma/\Gamma_0 - 1$  labels the relative corrections. The first two channels,  $e^-e^+\mu^-\mu^+$  and  $l^-l^+l^-l^+$ ,  $l = e, \mu$ , result from the decay  $H \rightarrow ZZ \rightarrow 4f$ . The partial widths for only electrons or muons in the final state are equal in the limit of vanishing external fermion masses, since for collinear-safe observables, such as the partial widths, the fermion-mass logarithms cancel. The corresponding lowest-order matrix elements are given in (2.11) and (2.13), respectively. The width for  $H \rightarrow l^-l^+l^-l^+$  is typically smaller by a factor 2, because it gets a factor 1/4 for identical particles in the final state and it proceeds in lowest order via two Feynman diagrams that are related by the exchange of two outgoing electrons and that have only a

	$M_H[\text{GeV}]$	140		170		200	
	$\Gamma_W[\text{GeV}]$	2.09052...		2.09054...		2.09055...	
	$\Gamma_Z[\text{GeV}]$	2.50278...		2.50287...		2.50292...	
H $\rightarrow$		$\Gamma[\text{MeV}]$	$\delta[\%]$	$\Gamma[\text{MeV}]$	$\delta[\%]$	$\Gamma[\text{MeV}]$	$\delta[\%]$
$e^-e^+\mu^-\mu^+$	corrected	0.0012628(5)	2.3	0.020162(7)	2.7	0.8202(2)	4.4
	lowest order	0.0012349(4)		0.019624(5)		0.78547(8)	
$l^-l^+l^-l^+$ $l = e, \mu$	corrected	0.0006692(2)	2.1	0.010346(3)	2.7	0.41019(8)	4.4
	lowest order	0.0006555(2)		0.010074(2)		0.39286(4)	
$\nu_e e^+ \mu^- \bar{\nu}_\mu$	corrected	0.04807(2)	3.7	4.3109(9)	6.2	12.499(3)	5.0
	lowest order	0.04638(1)		4.0610(7)		11.907(2)	
$\nu_l l^+ l^- \bar{\nu}_l$ $l = e, \mu$	corrected	0.04914(2)	3.7	4.344(1)	6.1	14.133(3)	5.0
	lowest order	0.04738(2)		4.0926(8)		13.458(2)	

Table 1: Partial decay widths for  $H \rightarrow 4\text{ leptons}$  including  $\mathcal{O}(\alpha)$  and  $\mathcal{O}(G_\mu^2 M_H^4)$  corrections and corresponding relative corrections for various decay channels and different Higgs masses.

small interference. The channel  $\nu_e e^+ \mu^- \bar{\nu}_\mu$  (2.12) results from the decay  $H \rightarrow WW \rightarrow 4f$ , while the last channel  $\nu_l l^+ l^- \bar{\nu}_l$  (2.14) receives contributions from both the decay into W and into Z bosons. The larger the Higgs mass, the larger is the decay width, because the available phase space grows.

In the two upper plots of Figure 7 we show the partial decay width for the final state  $\nu_e e^+ \mu^- \bar{\nu}_\mu$  as a function of the Higgs mass. The lower plots show the corrections relative to the lowest-order result. As already explained, we always normalize to the lowest-order result that already includes the  $\mathcal{O}(\alpha)$ -corrected gauge-boson width in the complex masses of the gauge bosons. A large fraction of the  $\mathcal{O}(\alpha)$  corrections is transferred to the lowest-order decay width by applying the  $G_\mu$  scheme. Thus, the corrections are at the order of 2–8% for moderate Higgs masses. However, for large Higgs masses the corrections become larger and reach about 13% at  $M_H = 700\text{ GeV}$ . In this region the leading two-loop corrections already amount to about 4%. Around the WW threshold at 160 GeV the Coulomb singularity, which originates from soft-photon exchange between the two slowly moving W bosons, is reflected in the shape of the curve. The influence of diagrams with a Higgs boson splitting into a virtual Z-boson pair (ZZ threshold) is visible at  $M_H \sim 2M_Z$ . At about  $2m_t$  the  $t\bar{t}$  threshold is visible.

For stable W or Z bosons, i.e. in the limit  $\Gamma_V \rightarrow 0$  ( $V = W, Z$ ), it is possible to define a narrow-width approximation (NWA) where the matrix elements factorize into the decay  $H \rightarrow VV$  and the subsequent decay of the gauge bosons into fermions. By definition the NWA is only applicable above the WW or ZZ threshold. However, its analytical structure and evaluation is considerably simpler than in the case of the full decay  $H \rightarrow WW/ZZ \rightarrow 4f$  with off-shell gauge bosons. Therefore, above threshold the NWA allows for an economic way of calculating relative  $\mathcal{O}(\alpha)$  corrections to the integrated

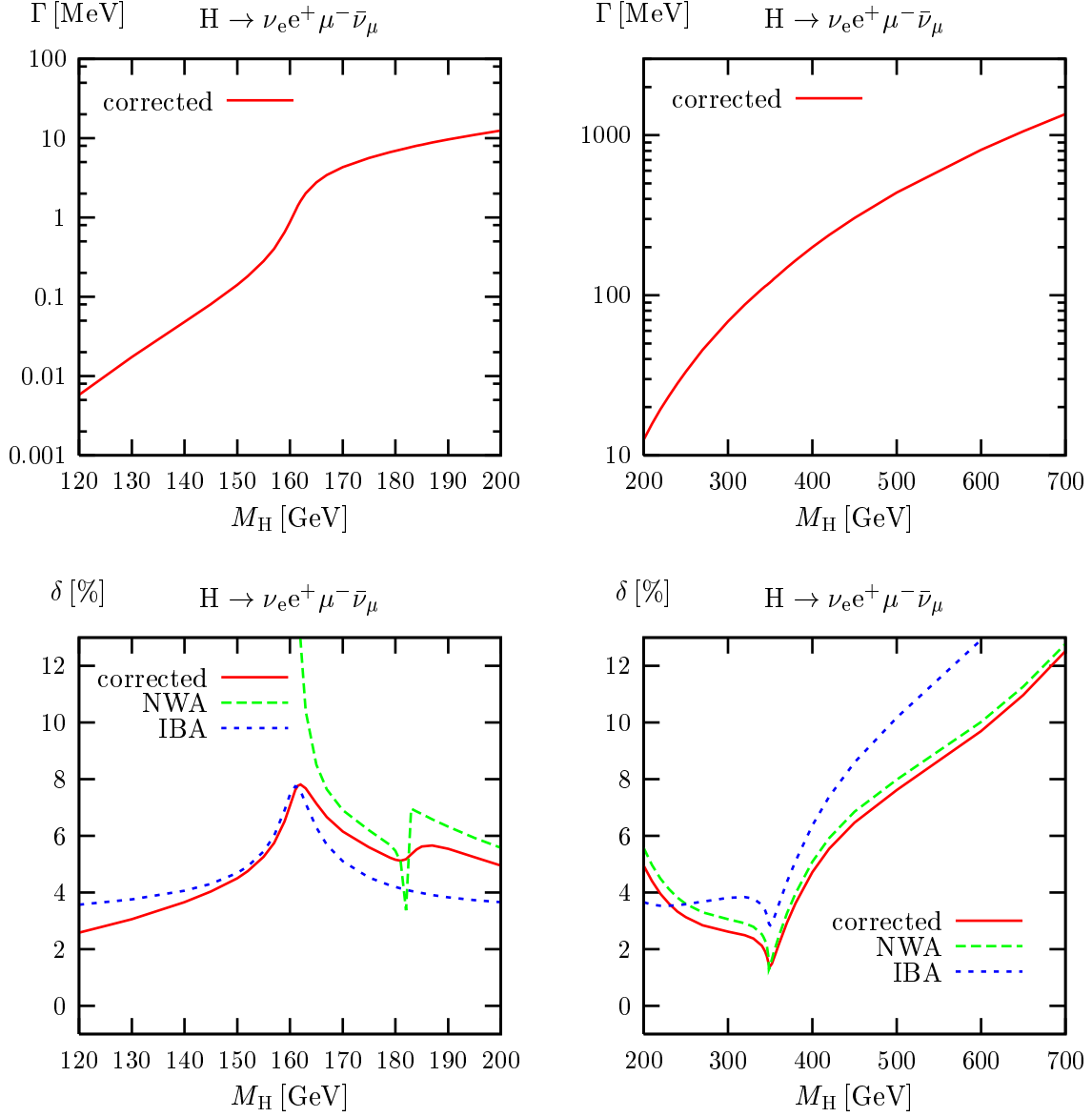


Figure 7: Partial decay width for  $H \rightarrow \nu_e e^+ \mu^- \bar{\nu}_\mu$  as a function of the Higgs mass. The upper plots show the absolute prediction including  $\mathcal{O}(\alpha)$  and  $\mathcal{O}(G_\mu^2 M_H^4)$  corrections, and the lower plots show the comparison of the corresponding relative corrections with the NWA and IBA.



decay width, while the lowest-order contribution may, of course, still take into account unstable gauge bosons. Following this line of thought, we define

$$\Gamma^{\text{NWA}} = \Gamma_0 \frac{\Gamma_1^{\text{NWA}}}{\Gamma_0^{\text{NWA}}}, \quad (7.5)$$

with

$$\Gamma_1^{\text{NWA}} = \Gamma_{\text{HVV},1} \frac{\Gamma_{Vf_1\bar{f}_2,1} \Gamma_{Vf_3\bar{f}_4,1}}{\Gamma_{V,1} \Gamma_{V,1}}, \quad (7.6)$$

and

$$\Gamma_0^{\text{NWA}} = \Gamma_{\text{HVV},0} \frac{\Gamma_{Vf_1\bar{f}_2,0} \Gamma_{Vf_3\bar{f}_4,0}}{\Gamma_{V,1} \Gamma_{V,1}}. \quad (7.7)$$

The indices “0” and “1” label lowest-order and  $\mathcal{O}(\alpha)$ -corrected results, respectively. The Higgs-mass-enhanced two-loop terms, described in Section 3.3, have also been included in  $\Gamma_{\text{HVV},1}$ . In order to be consistent we again use the  $\mathcal{O}(\alpha)$ -corrected total width for the gauge bosons in the denominators of the branching ratios in  $\Gamma_0^{\text{NWA}}$ . We note that we have rederived all necessary  $\mathcal{O}(\alpha)$  corrections entering the NWA; the hard-photon corrections to the decay  $\text{H} \rightarrow \text{WW}$  have been successfully checked against the expression given in Ref. [19]. The NWA is evaluated with real gauge-boson and top-quark masses.

A few GeV above the corresponding gauge-boson-pair threshold the NWA agrees with the complete corrections within 1%. Near  $M_{\text{H}} = 2M_{\text{Z}} \sim 180 \text{ GeV}$  the loop-induced ZZ threshold can be seen in the relative corrections to  $\text{H} \rightarrow \text{WW} \rightarrow \nu_{\text{e}} e^+ \mu^- \bar{\nu}_{\mu}$  shown in Figure 7. In the NWA this threshold leads to a singularity visible as a sharp peak; in the off-shell calculation in the complex-mass scheme this singular structure is smeared out, because the finite Z-boson width is taken into account. Since the ZZ threshold corresponds to the situation where two Z bosons become on shell in the loop, the latter description with the singularity regularized by a finite  $\Gamma_{\text{Z}}$  is closer to physical reality. An analogous situation can be seen near  $M_{\text{H}} = 2m_{\text{t}} \sim 350 \text{ GeV}$  for the  $\text{t}\bar{\text{t}}$  threshold with top quarks in the loops. Again the inclusion of the top decay width  $\Gamma_{\text{t}}$ , as done in the off-shell calculation, yields the better description. In Figure 7 we show also the relative corrections obtained in the IBA of (6.1). The Coulomb singularity and the  $\text{t}\bar{\text{t}}$  threshold are well described, and the full corrections are reproduced within  $\lesssim 2\%$  for Higgs masses below 400 GeV.

The plots in Figure 8 show the decay width and the relative correction for the final state  $e^- e^+ \mu^- \mu^+$ . The corrections are between 2% and 4% for moderate Higgs masses and rise to more than 10% for large Higgs masses. At a Higgs mass of about 160 GeV the influence of the WW threshold can be observed. As explained above, the behaviour of the corrections as a function of the Higgs mass is smooth, because the finite W-boson width is also used in the loop integrals. In contrast to the decay  $\text{H} \rightarrow \nu_{\text{e}} e^+ \mu^- \bar{\nu}_{\mu}$ , there is no Coulomb singularity in this channel because the Z boson is electrically neutral. The NWA reproduces the complete result within 0.5% not too close to the threshold. The IBA agrees with the complete calculation to better than 2% for not too large Higgs masses.

### 7.3 Comparison of partial widths with HDECAY

Predictions for the partial decay widths of the Higgs boson can also be obtained with various program packages, such as HDECAY [17]. HDECAY contains the lowest-order

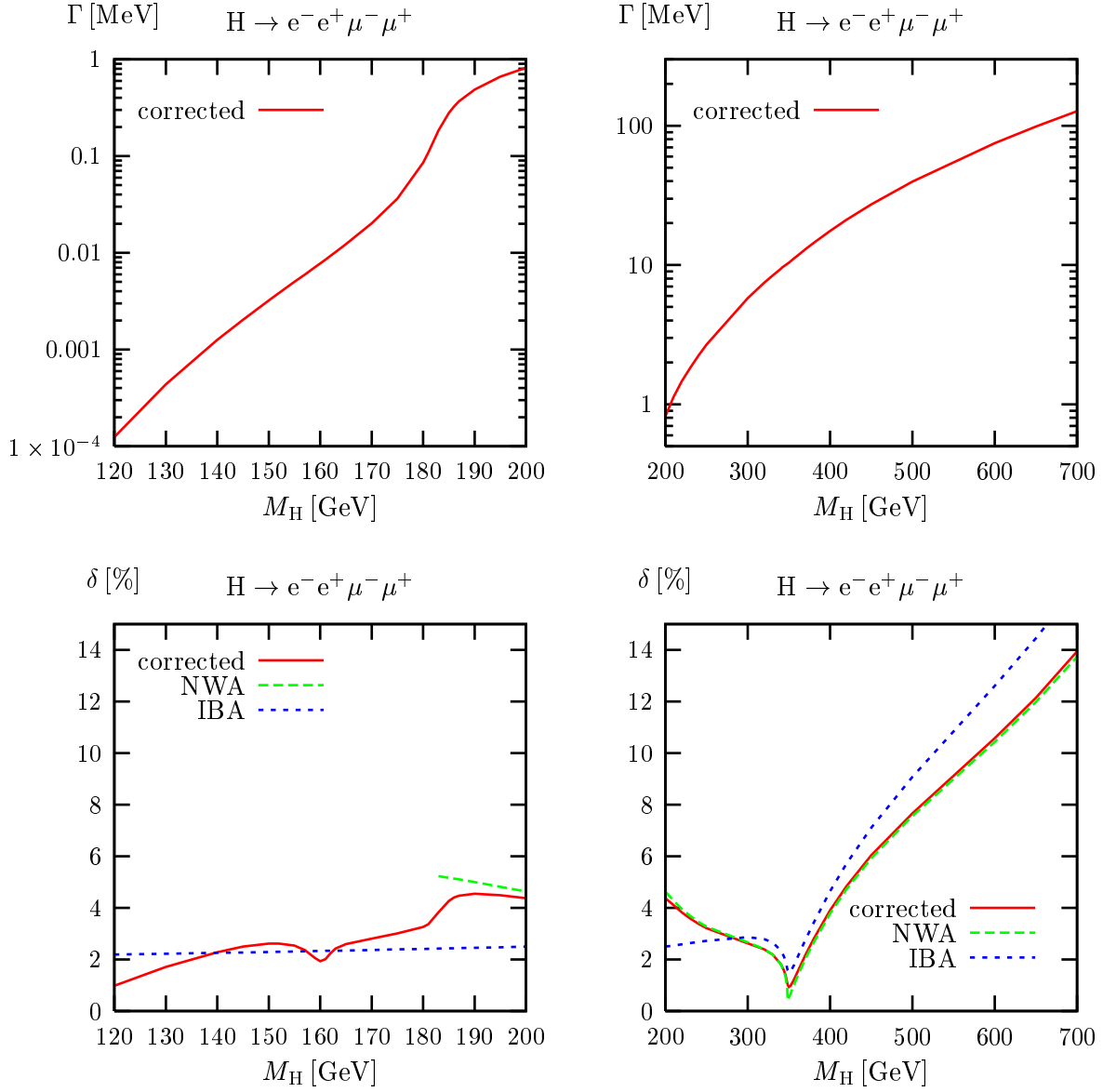


Figure 8: Partial decay width for  $H \rightarrow e^-e^+\mu^-\mu^+$  as a function of the Higgs mass. The upper plots show the absolute prediction including  $\mathcal{O}(\alpha)$  and  $\mathcal{O}(G_\mu^2 M_H^4)$  corrections, and the lower plots show the comparison of the corresponding relative corrections with the NWA and IBA.

decay width for  $H \rightarrow V^{(*)}V^{(*)}$  and the leading one-loop corrections  $\propto G_\mu M_H^2$  and two-loop corrections  $\propto G_\mu^2 M_H^4$ . In order to obtain the decay width for  $H \rightarrow WW/ZZ \rightarrow 4f$ , we define

$$\Gamma^{\text{HD}} = \Gamma_{\text{HVV}}^{\text{HD}} \frac{\Gamma_{Vf_1f_2,0}}{\Gamma_{V,1}} \frac{\Gamma_{Vf_3f_4,0}}{\Gamma_{V,1}}, \quad (7.8)$$

where  $\Gamma_{\text{HVV}}^{\text{HD}}$  is the decay width from HDECAY. In (7.8) the branching ratios of the gauge bosons are normalized in the same way (lowest order in the numerator, corrected total width in the denominator) as the effective branching ratios of our lowest-order predictions for the  $H \rightarrow VV \rightarrow 4f$  partial widths; otherwise a comparison would not be conclusive.

The comparison in Figure 9, where  $\Gamma^{\text{HD}}$  is shown relative to our complete lowest-order prediction, shows that HDECAY agrees with our lowest-order prediction below the decay threshold quite well. In this region  $\Gamma_{\text{HVV}}^{\text{HD}}$  consistently takes into account the off-shell effects of the gauge bosons. Above the threshold HDECAY neglects off-shell effects of the gauge bosons. For large  $M_H$  it follows our corrected result within a few per cent, because the dominant radiative corrections  $\propto G_\mu M_H^2$  and  $\propto G_\mu^2 M_H^4$ , which grow fast with increasing  $M_H$ , are included in both calculations. In the threshold region, off-shell effects are, however, very important. Here, the difference between the complete off-shell result and the Higgs width for on-shell gauge bosons amounts to more than 10%. In detail, HDECAY interpolates between the off-shell and on-shell results within a window of  $\pm 2$  GeV around threshold. The maxima in the HDECAY curves near the WW and ZZ thresholds in the upper and lower left plots of Figure 9, respectively, are artifacts originating from the on-shell phase space of the W or Z bosons above threshold. Approaching the threshold from above, the on-shell phase space, and thus the corresponding partial decay width, tends to zero. This feature is avoided in HDECAY by the interpolation. The described maxima in the HDECAY curves have nothing to do with the maximum of the correction near the WW threshold in the upper left plot, which is due to the Coulomb singularity.

## 7.4 Invariant-mass distributions

In Figure 10 we study the invariant-mass distribution of the fermion pairs resulting from the decay of the W bosons in the decay  $H \rightarrow \nu_e e^+ \mu^- \bar{\nu}_\mu$ . The plots on the l.h.s. show the distribution for  $\mu^- \bar{\nu}_\mu$  including corrections for  $M_H = 170$  GeV and  $M_H = 140$  GeV, i.e. for one value of  $M_H$  above and one below the WW threshold. The plots on the r.h.s. compare the relative corrections for  $\nu_e e^+$  and  $\mu^- \bar{\nu}_\mu$  both with and without photon recombination. The invariant mass  $M_{f\bar{f}'}$  is calculated from the sum of the momenta of the fermions  $f$  and  $f'$ . If no photon recombination is applied, always the bare momenta are taken. In the case of photon recombination the momentum of recombined photons is included in the invariant mass as described in Section 7.1.

For  $M_H = 170$  GeV, where the width is dominated by contributions where both intermediate W bosons are simultaneously resonant, the shape of the curves in Figure 10 can be understood as follows. If one of the fermions resulting from the decay of a resonant W boson emits a photon, the invariant mass  $M_{f\bar{f}'}$  is reduced, giving rise to an enhancement for small invariant masses. Without photon recombination these positive corrections are large due to the appearance of logarithms of the small fermion masses. As the electron mass is smaller, the corresponding logarithms yield a larger contribution. If photon recombination is applied, events are rearranged from small invariant masses

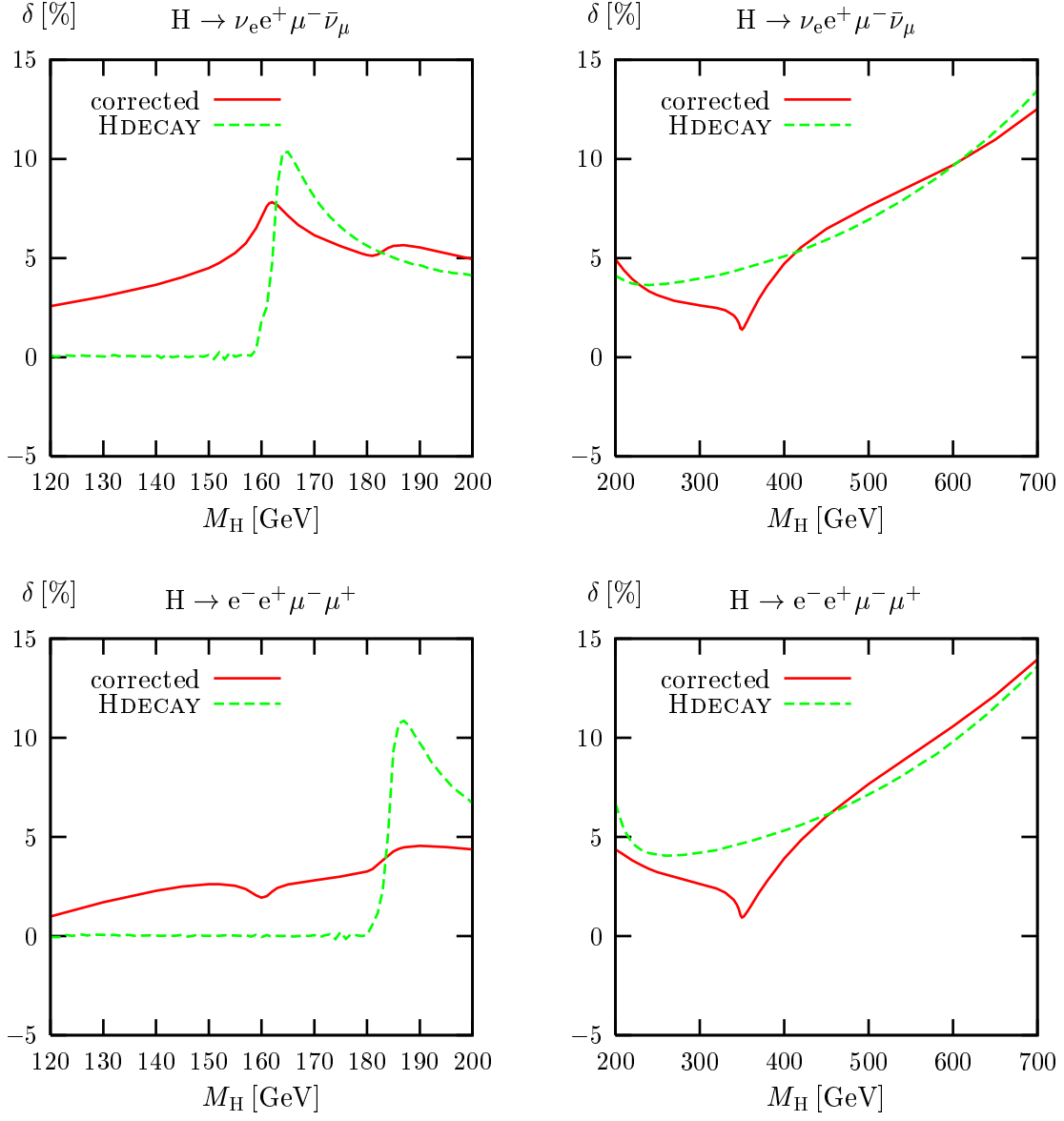


Figure 9: Predictions for the partial decay widths for  $H \rightarrow \nu_e e^+ \mu^- \bar{\nu}_\mu$  and  $H \rightarrow e^- e^+ \mu^- \mu^+$  obtained with the program HDECAY normalized to the complete lowest-order decay width. The corrections shown in Figures 7 and 8 are included for comparison.

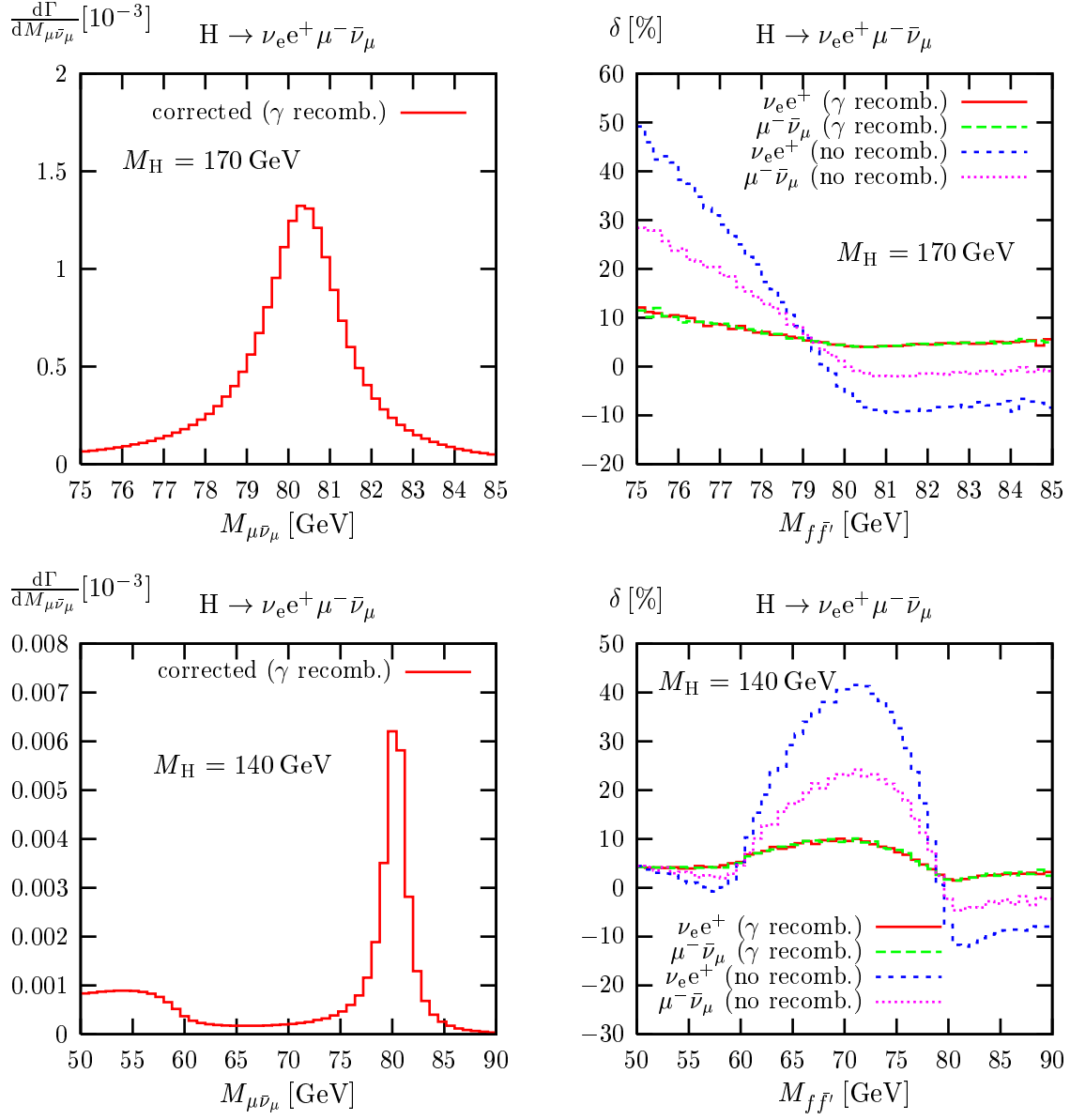


Figure 10: Distribution in the invariant mass of the  $\mu^- \bar{\nu}_\mu$  (l.h.s.) pair and relative corrections to the distributions in the invariant masses of the  $\nu_e e^+$  and  $\mu^- \bar{\nu}_\mu$  pairs (r.h.s.) in the decay  $H \rightarrow \nu_e e^+ \mu^- \bar{\nu}_\mu$  for  $M_H = 170$  GeV and  $M_H = 140$  GeV.

to large invariant masses. In this case, the observable is inclusive, i.e. the fermion mass logarithms cancel owing to the KLN theorem, and the  $\nu_e e^+$  and  $\mu^- \bar{\nu}_\mu$  distributions do not differ. The analogous phenomenon has, e.g., been discussed for the related resonance processes  $e^+ e^- \rightarrow WW \rightarrow 4 \text{ leptons}$  [ 59, 60] and  $\gamma\gamma \rightarrow WW \rightarrow 4f$  [ 33].

For  $M_H = 140 \text{ GeV}$ , i.e. below the threshold, only one W boson can become on shell. Thus, there is still a resonance around  $M_{f\bar{f}'} \sim M_W$ , but also an enhancement below an invariant mass of  $M_H - M_W \sim 60 \text{ GeV}$ , where the other decaying W boson can become resonant. Near the resonance at  $M_{f\bar{f}'} \sim M_W$  the corrections look similar to the doubly-resonant case discussed for  $M_H = 170 \text{ GeV}$  above. The same redistribution of events from higher to lower invariant mass due to FSR happens as explained above. Between  $M_W$  and  $M_H - M_W$  none of the W bosons is resonant, and the contribution to the lowest-order width is small. Therefore, owing to the redistribution of events via photon emission the relative corrections are large in this regime. Below  $M_H - M_W$ , where the other W boson can become resonant, qualitatively the same FSR effects are visible as in the vicinity of the resonance at  $M_W$ : apart from a constant positive off-set in the relative corrections, events are distributed from the right to the left of the maximum.

Figure 11 shows the corresponding invariant-mass distributions for the decay  $H \rightarrow e^- e^+ \mu^- \mu^+$  with  $M_H = 200 \text{ GeV}$  and  $M_H = 170 \text{ GeV}$ . The generic features of the plots are similar to the decay into W bosons. For  $M_H = 200 \text{ GeV}$ , i.e. above the ZZ threshold, there is a resonance region around  $M_Z$ , and the corrections become large in the non-collinear-safe case. Photon recombination rearranges the events, so that the fermion logarithms cancel. For Higgs masses below the ZZ threshold, such as for  $M_H = 170 \text{ GeV}$ , one Z boson or the other is resonant for  $M_{f\bar{f}} \sim M_Z$  or  $M_{f\bar{f}} \lesssim M_H - M_Z$ , respectively. The shape and the large size of the corrections are due to collinear FSR as explained above. In Ref. [ 13] it was pointed out that the kinematical threshold near  $M_H - M_Z$  where the other Z boson can become on shell, which is at  $M_{f\bar{f}} \sim 80 \text{ GeV}$  in Figure 11, can be used to verify the spin of the Higgs boson. While the rise of the width near this threshold is proportional to  $\beta \propto \sqrt{[1 - (M_Z + M_{f\bar{f}})^2/M_H^2][1 - (M_Z - M_{f\bar{f}})^2/M_H^2]}$  for a spin-0 particle, it would be proportional to  $\beta^3$  for a spin-1 particle. Figure 11 shows that the radiative corrections influence the slope at the kinematical threshold.

Finally, in Figure 12 we investigate the influence of the contribution  $\delta_{\text{FSR}}$  of higher-order FSR to the complete relative correction  $\delta$  on the invariant-mass distribution of  $\mu^- \bar{\nu}_\mu$  and  $\mu^- \mu^+$  in the decays  $H \rightarrow \nu_e e^+ \mu^- \bar{\nu}_\mu$  and  $H \rightarrow e^- e^+ \mu^- \mu^+$ . The invariant mass is defined via the momenta of the fermions alone, i.e. without photon recombination. If photon recombination was applied, the leading logarithmic FSR corrections, as described in Section 4.3, would vanish completely. Subtracting the  $\mathcal{O}(\alpha)$  terms (4.16) with (4.17) from (4.11) with the structure functions (4.12) yields the contribution that is beyond  $\mathcal{O}(\alpha)$ . In Figure 12 the impact of this contribution is studied revealing corrections of up to 4% in regions where the lowest-order result is relatively small. Figure 12 also shows the comparison between the structure function with and without the exponentiation of the soft-photon parts in (4.12) and (4.14), respectively. The difference is beyond  $\mathcal{O}(\alpha^3)$  and turns out to be tiny.

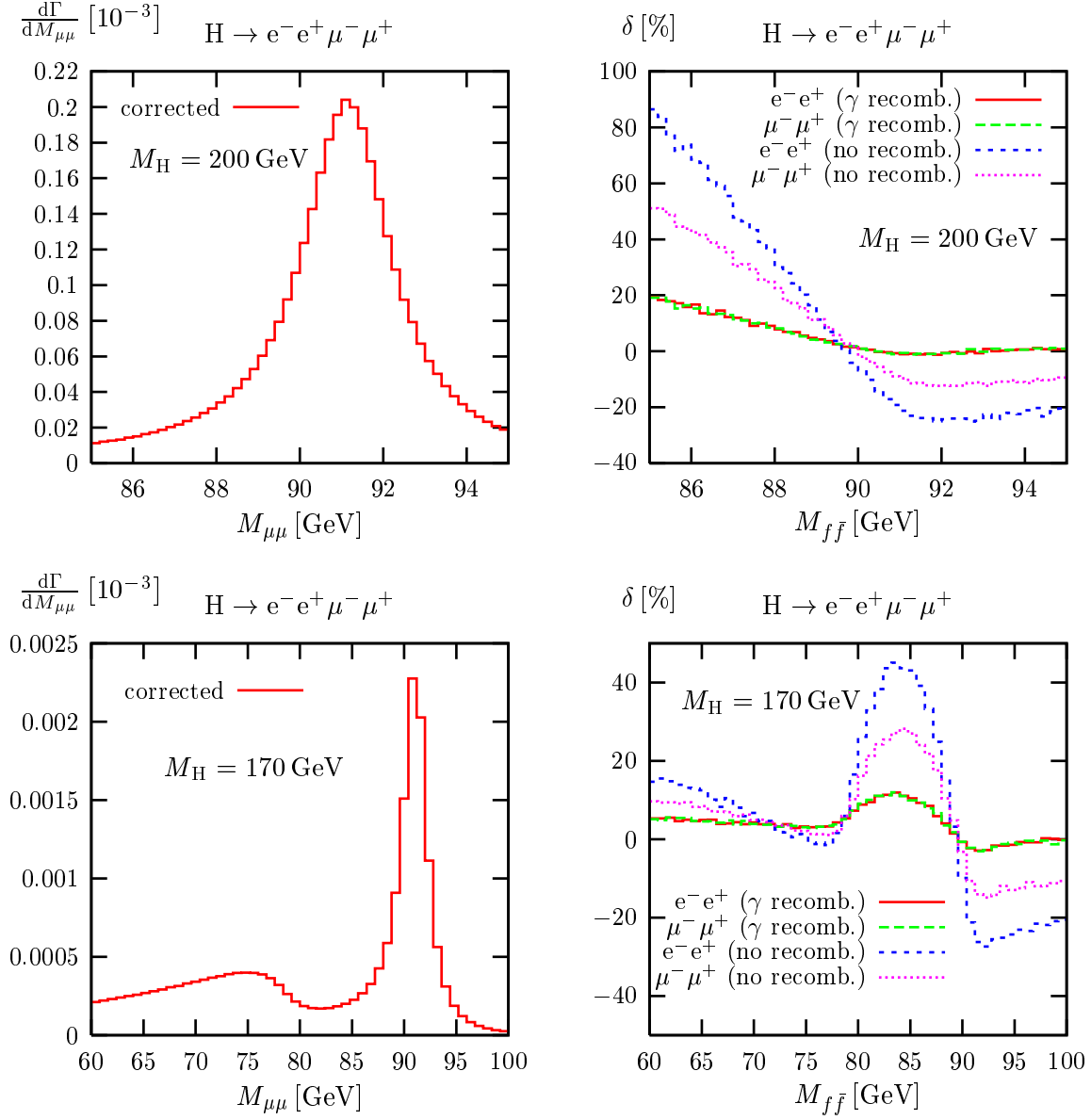


Figure 11: Distribution in the invariant mass of the  $\mu^- \mu^+$  pair (l.h.s.) and relative corrections to the distributions in the invariant masses of the  $e^- e^+$  and  $\mu^- \mu^+$  pairs (r.h.s.) in the decay  $H \rightarrow e^- e^+ \mu^- \mu^+$  for  $M_H = 200$  GeV and  $M_H = 170$  GeV.

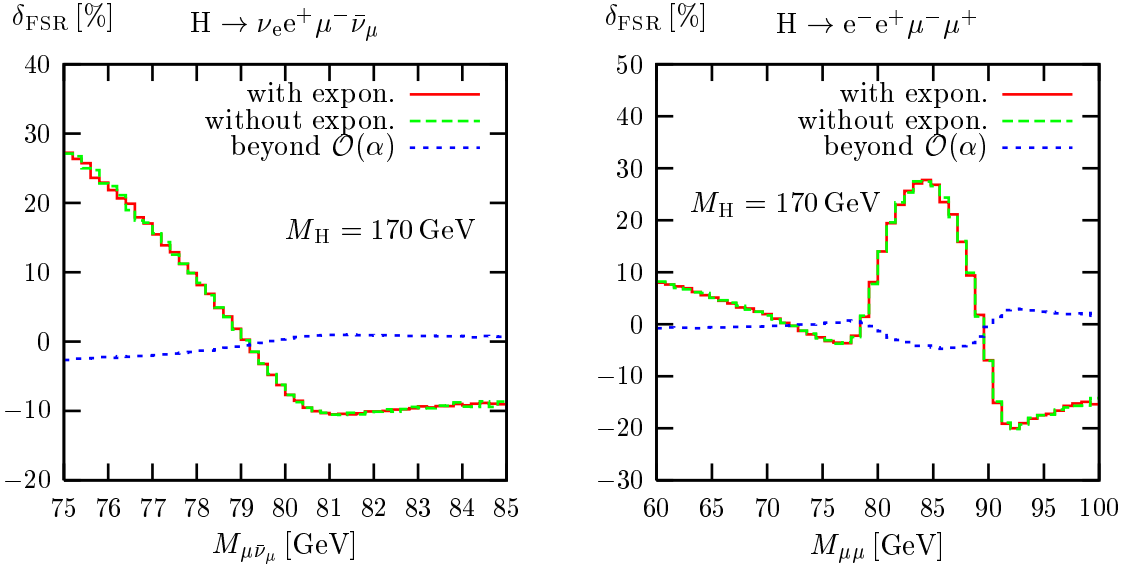


Figure 12: Influence of the leading logarithmic terms of FSR on the invariant-mass distribution of  $\mu^-\bar{\nu}_\mu$  and  $\mu^-\mu^+$  in the decays  $H \rightarrow \nu_e e^+ \mu^- \bar{\nu}_\mu$  and  $H \rightarrow e^- e^+ \mu^- \mu^+$ . The different curves correspond to the result with exponentiation, without exponentiation, and to the sum of  $\alpha^2$  and  $\alpha^3$  terms, which are labelled “beyond  $\mathcal{O}(\alpha)$ ”.

## 7.5 Angular distributions

The investigation of angular correlations between the fermionic decay products is an essential means of testing the properties of the Higgs boson. In Refs. [12, 13] it was demonstrated how the spin of the Higgs boson can be determined by looking at the angle between the decay planes of the Z bosons in the decay  $H \rightarrow ZZ$ . This angle can be defined by

$$\cos \phi' = \frac{(\mathbf{k}_{12} \times \mathbf{k}_1)(\mathbf{k}_{12} \times \mathbf{k}_3)}{|\mathbf{k}_{12} \times \mathbf{k}_1||\mathbf{k}_{12} \times \mathbf{k}_3|},$$

$$\text{sgn}(\sin \phi') = \text{sgn}\{\mathbf{k}_{12} \cdot [(\mathbf{k}_{12} \times \mathbf{k}_1) \times (\mathbf{k}_{12} \times \mathbf{k}_3)]\}, \quad (7.9)$$

where  $\mathbf{k}_{12} = \mathbf{k}_1 + \mathbf{k}_2$ . The l.h.s. of Figure 13 shows the differential decay width for  $H \rightarrow e^- e^+ \mu^- \mu^+$  as a function of  $\phi'$  revealing a  $\cos 2\phi'$  term. As was noticed in Refs. [12, 13], this term would be proportional to  $(-\cos 2\phi')$  if the Higgs boson was a pseudo-scalar.

Note that for non-photonic events the definition of  $\phi'$  coincides with the definition given in Ref. [59] where  $(-\mathbf{k}_{34} \times \mathbf{k}_3)$  with  $\mathbf{k}_{34} = \mathbf{k}_3 + \mathbf{k}_4$  was used instead of  $(\mathbf{k}_{12} \times \mathbf{k}_3)$ . Explicitly,  $\phi$  was defined by

$$\cos \phi = \frac{(\mathbf{k}_{12} \times \mathbf{k}_1)(-\mathbf{k}_{34} \times \mathbf{k}_3)}{|\mathbf{k}_{12} \times \mathbf{k}_1||-\mathbf{k}_{34} \times \mathbf{k}_3|},$$

$$\text{sgn}(\sin \phi) = \text{sgn}\{\mathbf{k}_{12} \cdot [(\mathbf{k}_{12} \times \mathbf{k}_1) \times (-\mathbf{k}_{34} \times \mathbf{k}_3)]\}. \quad (7.10)$$

However, this definition yields large negative contributions at  $\phi = 0^\circ$  and  $\phi = 180^\circ$ . As was explained in Ref. [59], this is an effect of the suppressed phase space in the real



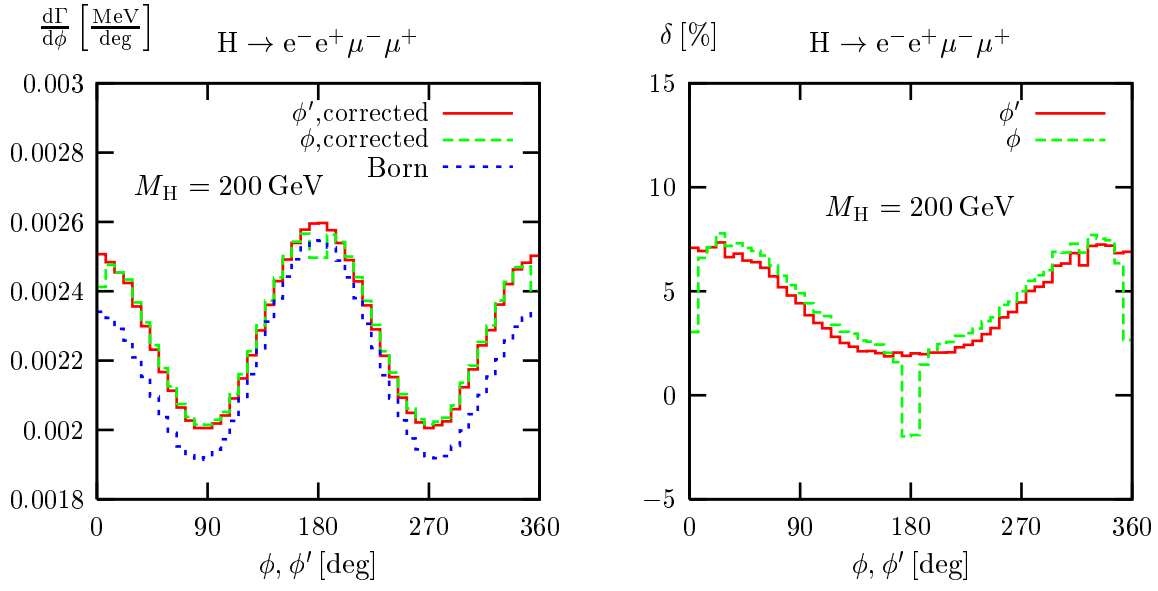


Figure 13: Distribution in the angle between the  $Z \rightarrow l^-l^+$  decay planes in the decay  $H \rightarrow e^-e^+\mu^-\mu^+$  (l.h.s.) and corresponding relative corrections (with photon recombination) (r.h.s.) for  $M_H = 200$  GeV.

corrections. At  $\phi = 0^\circ$  and  $\phi = 180^\circ$  the phase space for photonic events shrinks to the configurations where the photon is either soft or lies in the decay plane of the gauge bosons. Thus, the negative contributions from the virtual corrections are not fully compensated by the real corrections. Using  $\mathbf{k}_{12} \times \mathbf{k}_3$  as in (7.9) avoids this suppression and gives rise to a smooth dependence of the corrections on  $\phi$  as can be seen on the r.h.s. of Figure 13 which shows the relative corrections for  $\phi$  and  $\phi'$  in the decay  $H \rightarrow e^-e^+\mu^-\mu^+$ . Since the difference of  $\phi$  and  $\phi'$  is only due to photons, this, again, emphasizes the influence of the photon treatment.

In contrast to the invariant-mass distribution of Figure 10, photon recombination does not produce any significant effect for the observables  $\phi, \phi'$ . This is because adding a soft or collinear photon to a fermion momentum does not change its direction significantly and, thus, has only a small influence on the angles  $\phi, \phi'$ .

The distribution in the decay angle of the  $\mu^-$  relative to the corresponding Z boson in the decay  $H \rightarrow e^-e^+\mu^-\mu^+$  is shown in Figure 14. The angle is defined in the rest frame of the Z boson. Since the Z bosons resulting from Higgs decay are preferably longitudinally polarized, the distribution involves a component proportional to  $\sin^2 \theta_{Z\mu^-}$ . The relative corrections which are shown in the plot on the r.h.s. reveal a strong enhancement in the forward and backward direction if no recombination is applied. This enhancement is due to events where the  $\mu^+$  emits a collinear photon and has only a small energy left. Since the momentum of the Z boson is defined via its decay fermions, it has almost the same momentum as the  $\mu^-$ . This configuration is enhanced by collinear logarithms which are not compensated by virtual contributions. After applying photon recombination, the momentum of the Z boson is defined via the sum of the fermion and photon momenta.

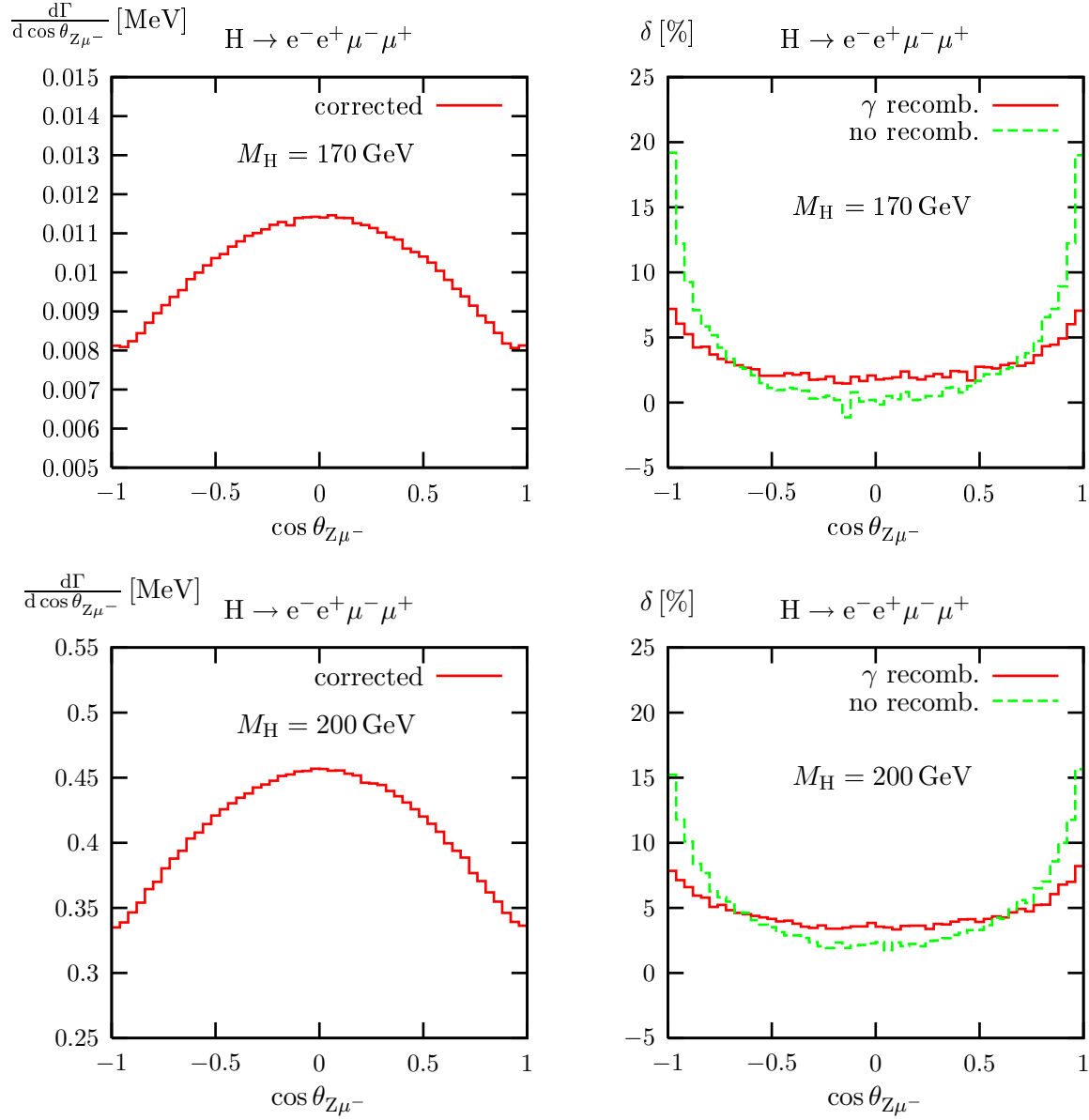


Figure 14: Distribution in the angle between the  $\mu^-$  and the corresponding Z boson in the rest frame of the Z boson (l.h.s.) and corresponding relative corrections with and without photon recombination (r.h.s.) in the decay  $H \rightarrow e^- e^+ \mu^- \mu^+$  for  $M_H = 170$  GeV and  $M_H = 200$  GeV.

Thus, the  $\mu^-$  is not necessarily collinear to the Z boson anymore, and events are rearranged to smaller  $|\cos \theta_{Z\mu^-}|$  giving rise to a flatter distribution.

Next, we consider the distribution in the angle between two fermions. In the case of  $H \rightarrow WW$  the angle between the charged fermions can be used to discriminate the Higgs signal events from background events [2], because the fermions are emitted preferably in the same direction. This can be understood as follows. At leading order, the only non-vanishing helicity amplitudes for  $H \rightarrow WW$  are those with equal-helicity W bosons. Since W bosons only couple to left-handed particles and due to angular momentum conservation, particles (anti-particles) are emitted preferably in the forward direction of transverse W bosons with negative (positive) helicity, and anti-particles (particles) in the backward direction. As, close to threshold, 2/3 of the W bosons are transverse and as the W bosons fly in opposite directions, a particle and an anti-particle of their decay products will be emitted preferably in the same direction, resulting in small angles between these particles.

In the decay  $H \rightarrow \nu_e e^+ \mu^- \bar{\nu}_\mu$  neither the Higgs-boson nor the W-boson momenta can be reconstructed from the decay products. The distribution in the angle between the  $e^+$  and  $\mu^-$  can, thus, only be studied upon including the Higgs-production process. If the Higgs boson was, however, produced without transverse momentum, or if the transverse momentum was known, the angle between  $e^+$  and  $\mu^-$  in the plane perpendicular to the beam axis could be studied without knowledge of the production process. We define the transverse angle between  $e^+$  and  $\mu^-$  in the frame where  $\mathbf{k}_{H,T} = 0$  as

$$\cos \phi_{e\mu,T} = \frac{\mathbf{k}_{2,T} \cdot \mathbf{k}_{3,T}}{|\mathbf{k}_{2,T}| |\mathbf{k}_{3,T}|},$$

$$\text{sgn}(\sin \phi_{e\mu,T}) = \text{sgn}\{\mathbf{e}_z \cdot (\mathbf{k}_{2,T} \times \mathbf{k}_{3,T})\}, \quad (7.11)$$

where  $\mathbf{k}_{i,T}$  are the transverse components of the fermion momenta w.r.t. the unit vector  $\mathbf{e}_z$ , which could be identified with the beam direction of a Higgs production process.

The corresponding distribution, together with the influence of the corrections, is shown in Figure 15. The enhancement for small angles, which was explained above, is transferred to the distribution of the transverse angle  $\phi_{e\mu,T}$ . Since the photon recombination does not change the direction of the fermions, it does not have any visible effect on the relative corrections.

Finally, we investigate the distribution of the angle between  $e^-$  and  $\mu^-$  in the decay  $H \rightarrow e^- e^+ \mu^- \mu^+$ . We prefer to choose the angle between two fermions with the same charge because this constitutes an unambiguous choice in the decay  $H \rightarrow \mu^- \mu^+ \mu^- \mu^+$ . Figure 16 shows the tendency that the fermions are emitted in opposite directions for the same reason as explained above. However, this feature is not as pronounced as in  $H \rightarrow \nu_e e^+ \mu^- \bar{\nu}_\mu$ , because Z bosons do also couple to right-handed fermions so that one Z boson might decay into a left-handed fermion and the other into a right-handed fermion. The radiative corrections tend to reduce the enhancement in forward direction and do not depend on photon recombination.

## 8 Conclusions

The decays of the Standard Model Higgs boson into four leptons via a W-boson or Z-boson pair lead to experimental signatures at the LHC that are both important for the

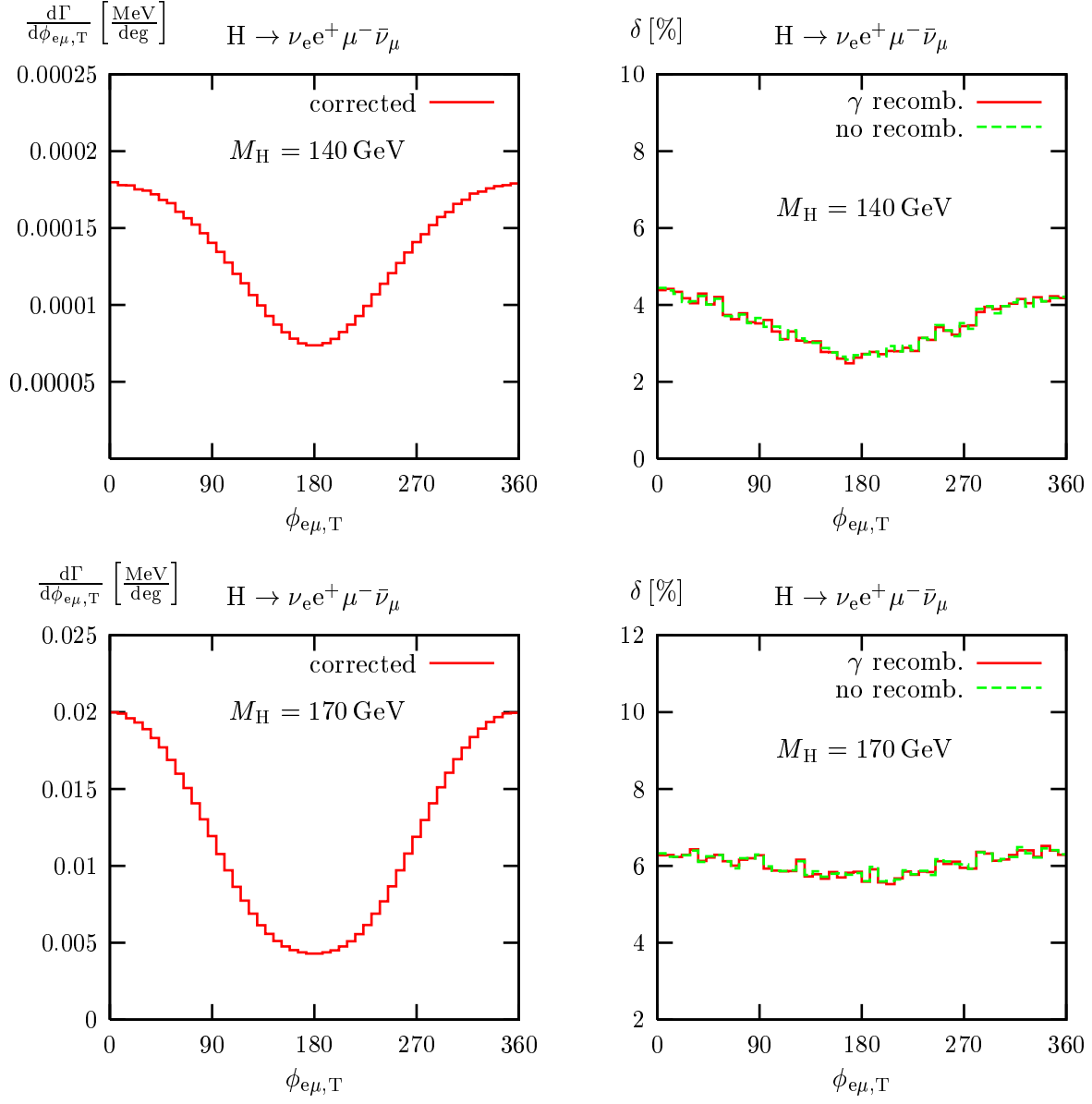


Figure 15: Distribution in the transverse angle between  $e^+$  and  $\mu^-$  including corrections (l.h.s.) and corresponding relative corrections (r.h.s.) with and without applying photon recombination in the decay  $H \rightarrow \nu_e e^+ \mu^- \bar{\nu}_\mu$  for  $M_H = 140 \text{ GeV}$  and  $M_H = 170 \text{ GeV}$ .

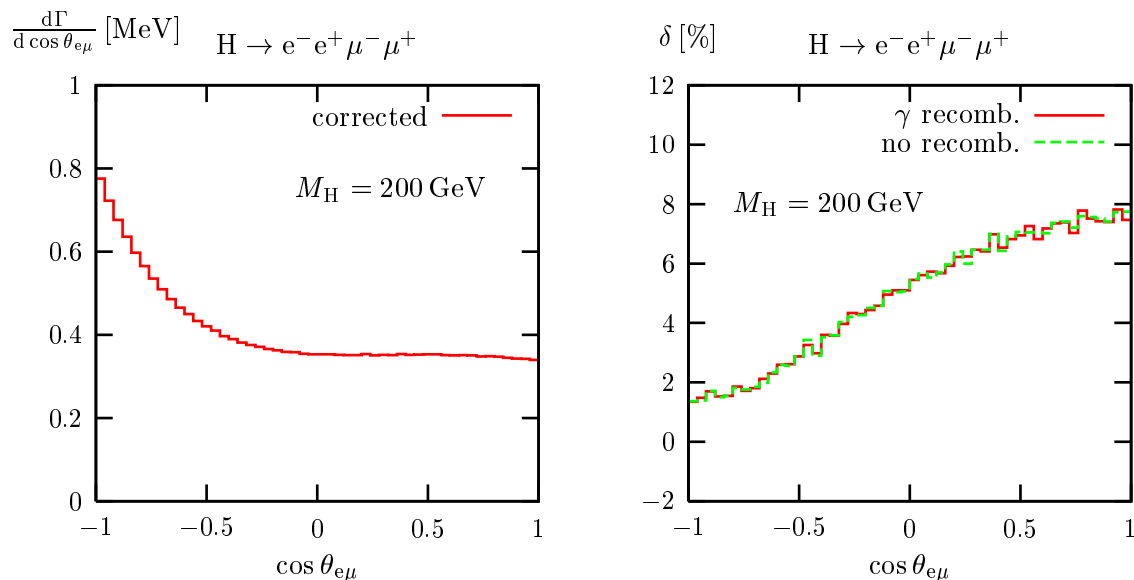


Figure 16: Distribution in the angle between  $e^-$  and  $\mu^-$  including corrections (l.h.s.) and corresponding relative corrections (r.h.s.) with and without applying photon recombination in the decay  $H \rightarrow e^-e^+\mu^-\mu^+$  for  $M_H = 200$  GeV.

search for the Higgs boson and for studying its properties. To exploit this possibility a Monte Carlo event generator for the decays  $H \rightarrow WW/ZZ \rightarrow 4\text{ leptons}$  is needed that properly accounts for the relevant radiative corrections, in order to achieve the necessary precision in predictions. PROPHECY4F is an event generator dedicated to this task. We have shown first results of this generator and described the underlying calculation.

In detail, we have presented the complete electroweak radiative corrections of  $\mathcal{O}(\alpha)$  to the decays  $H \rightarrow 4\text{ leptons}$ , supplemented by corrections beyond  $\mathcal{O}(\alpha)$  originating from heavy-Higgs effects and final-state radiation. The intermediate W- and Z-boson resonances are treated in the so-called complex-mass scheme, which fully preserves gauge invariance and does not employ any type of expansion or on-shell approximation for the intermediate gauge-boson resonances. Consequently, the calculation is equally valid above, in the vicinity of, and below the WW and ZZ thresholds.

The corrections to partial decay widths typically amount to some per cent and increase with growing Higgs mass  $M_H$ , reaching about 8% at  $M_H \sim 500$  GeV. This statement, however, applies only if the lowest-order decay widths are already evaluated with the full off-shell effects of the intermediate W and Z bosons, in particular near and below the WW and ZZ thresholds. The on-shell (narrow-width) approximation for the corrections is good within 0.5–1% of the width for Higgs masses sufficiently above the corresponding gauge-boson pair threshold, as long as the lowest-order prediction consistently includes the off-shell effects of the gauge bosons. For  $H \rightarrow WW \rightarrow 4f$  the narrow-width approximation fails by about 10% for Higgs masses that are only 2 GeV above the WW threshold, because the instability of the W bosons significantly influences the Coulomb singularity near threshold. Only a calculation that keeps the full off-shellness of the W and Z bosons can describe the threshold regions properly. We have given a simple improved Born ap-

proximation for the partial widths that reproduces the full calculation within  $\lesssim 2\%$  for Higgs masses below 400 GeV. In this regime our complete calculation has a theoretical uncertainty below 1%. For larger Higgs masses we expect that unknown two-loop corrections that are enhanced by  $G_\mu M_H^2$  deteriorate the accuracy. Finally, for  $M_H \gtrsim 700$  GeV it is well known that perturbative predictions become questionable in general.

For angular distributions, which are important in the verification of the discrete quantum numbers of the Higgs boson, the corrections are of the order of 5–10% and distort the shapes. For invariant-mass distributions of fermion pairs, which are relevant for the reconstruction of the gauge bosons, the situation is similar to gauge-boson pair production processes such as  $e^+e^- \rightarrow WW \rightarrow 4$  fermions, i.e. the corrections can reach several tens of per cent depending on the treatment of photon radiation.

In its present version the Monte Carlo event generator PROPHECY4F deals with fully leptonic final states, a situation most relevant for the LHC. The generalization to semi-leptonic and hadronic final states, including a proper description of QCD corrections, will be described in a forthcoming publication.

## Acknowledgements

We thank M. Spira for helpful discussions about HDECAY.

## References

- [1] E. W. N. Glover, J. Ohnemus and S. S. D. Willenbrock, Phys. Rev. D **37** (1988) 3193;  
V. D. Barger, G. Bhattacharya, T. Han and B. A. Kniehl, Phys. Rev. D **43** (1991) 779;  
V. D. Barger, R. J. N. Phillips and D. Zeppenfeld, Phys. Lett. B **346** (1995) 106 [hep-ph/9412276];  
D. L. Rainwater and D. Zeppenfeld, Phys. Rev. D **60** (1999) 113004 [Erratum-ibid. D **61** (2000) 099901] [hep-ph/9906218];  
N. Kauer, T. Plehn, D. L. Rainwater and D. Zeppenfeld, Phys. Lett. B **503** (2001) 113 [hep-ph/0012351].
- [2] M. Dittmar and H. K. Dreiner, Phys. Rev. D **55** (1997) 167 [hep-ph/9608317].
- [3] S. Asai *et al.*, Eur. Phys. J. C **32S2** (2004) 19 [hep-ph/0402254];  
S. Abdullin *et al.*, Eur. Phys. J. C **39S2** (2005) 41.
- [4] L. Zivkovic, Czech. J. Phys. **54** (2004) A73.
- [5] ATLAS Collaboration, Technical Design Report, CERN-LHCC 99-14 (May 1999);  
CMS Collaboration, Technical Proposal, CERN-LHCC 94-38 (Dec. 1994).
- [6] K. A. Assamagan *et al.* [Higgs Working Group Collaboration], proceedings of the 3rd Les Houches Workshop: “Physics at TeV Colliders”, Les Houches, 2003, hep-ph/0406152.

- [7] C. Buttar *et al.* [SMH Working Group Collaboration] QCD, EW, and Higgs working group report of the workshop “Physics at TeV Colliders”, Les Houches, May 2005, hep-ph/0604120.
- [8] J. A. Aguilar-Saavedra *et al.*, TESLA Technical Design Report Part III: Physics at an  $e^+e^-$  Linear Collider, hep-ph/0106315.
- [9] T. Abe *et al.* [American Linear Collider Working Group Collaboration], in *Proc. of the APS/DPF/DPB Summer Study on the Future of Particle Physics (Snowmass 2001)* ed. R. Davidson and C. Quigg, SLAC-R-570, *Resource book for Snowmass 2001*, [hep-ex/0106055, hep-ex/0106056, hep-ex/0106057, hep-ex/0106058].
- [10] K. Abe *et al.* [ACFA Linear Collider Working Group Collaboration], ACFA Linear Collider Working Group report, [hep-ph/0109166].
- [11] N. Meyer and K. Desch, Eur. Phys. J. C **35** (2004) 171.
- [12] C. A. Nelson, Phys. Rev. D **37** (1988) 1220;  
A. Soni and R. M. Xu, Phys. Rev. D **48** (1993) 5259 [hep-ph/9301225];  
D. Chang, W. Y. Keung and I. Phillips, Phys. Rev. D **48** (1993) 3225 [hep-ph/9303226];  
A. Skjold and P. Osland, Phys. Lett. B **311** (1993) 261 [hep-ph/9303294];  
V.D. Barger, K.M. Cheung, A. Djouadi, B.A. Kniehl and P.M. Zerwas, Phys. Rev. D **49** (1994) 79 [hep-ph/9306270];  
T. Arens and L. M. Sehgal, Z. Phys. C **66** (1995) 89 [hep-ph/9409396];  
C. P. Buszello, I. Fleck, P. Marquard and J. J. van der Bij, Eur. Phys. J. C **32** (2004) 209 [hep-ph/0212396].
- [13] S. Y. Choi, D. J. Miller, M. M. Mühlleitner and P. M. Zerwas, Phys. Lett. B **553** (2003) 61 [hep-ph/0210077].
- [14] G. Pocsik and T. Torma, Z. Phys. C **6** (1980) 1;  
T. G. Rizzo, Phys. Rev. D **22** (1980) 722;  
W. Y. Keung and W. J. Marciano, Phys. Rev. D **30** (1984) 248.
- [15] R. N. Cahn, Rept. Prog. Phys. **52** (1989) 389;  
B. A. Kniehl, Phys. Lett. B **244** (1990) 537;  
A. Grau, G. Panchieri and R. J. N. Phillips, Phys. Lett. B **251** (1990) 293;  
E. Gross, G. Wolf and B. A. Kniehl, Z. Phys. C **63** (1994) 417 [Erratum-ibid. C **66** (1995) 321] [hep-ph/9404220].
- [16] A. Djouadi, hep-ph/0503172.
- [17] A. Djouadi, J. Kalinowski and M. Spira, Comput. Phys. Commun. **108** (1998) 56 [hep-ph/9704448].
- [18] J. Fleischer and F. Jegerlehner, Phys. Rev. D **23** (1981) 2001;  
B.A. Kniehl, Nucl. Phys. B **352** (1991) 1;  
D.Y. Bardin, P.K. Khristova and B.M. Vilensky, Sov. J. Nucl. Phys. **54** (1991) 833 [Yad. Fiz. **54** (1991) 1366].

- [19] B.A. Kniehl, Nucl. Phys. B **357** (1991) 439.
- [20] B. A. Kniehl and M. Spira, Z. Phys. C **69** (1995) 77 [hep-ph/9505225];  
B. A. Kniehl and M. Steinhauser, Phys. Lett. B **365** (1996) 297 [hep-ph/9507382];  
A. Djouadi, P. Gambino and B. A. Kniehl, Nucl. Phys. B **523** (1998) 17 [hep-ph/9712330].
- [21] B. A. Kniehl and M. Steinhauser, Nucl. Phys. B **454** (1995) 485 [hep-ph/9508241].
- [22] A. Ghinculov, Nucl. Phys. B **455** (1995) 21 [hep-ph/9507240].
- [23] A. Frink, B. A. Kniehl, D. Kreimer and K. Riesselmann, Phys. Rev. D **54** (1996) 4548 [hep-ph/9606310].
- [24] C. M. Carloni Calame, M. Moretti, G. Montagna, O. Nicrosini, F. Piccinini and A. D. Polosa, Nucl. Phys. Proc. Suppl. **157** (2006) 73 [hep-ph/0604033].
- [25] A. Bredenstein, A. Denner, S. Dittmaier and M.M. Weber, Nucl. Phys. Proc. Suppl. **157** (2006) 63 [hep-ph/0604033].
- [26] G. Bélanger, F. Boudjema, J. Fujimoto, T. Ishikawa, T. Kaneko, K. Kato and Y. Shimizu, Nucl. Phys. Proc. Suppl. **116** (2003) 353 [hep-ph/0211268] and Phys. Lett. B **559** (2003) 252 [hep-ph/0212261].
- [27] A. Denner, S. Dittmaier, M. Roth and M. M. Weber, Phys. Lett. B **560** (2003) 196 [hep-ph/0301189] and Nucl. Phys. B **660** (2003) 289 [hep-ph/0302198].
- [28] A. Denner, S. Dittmaier, M. Roth and L. H. Wieders, Phys. Lett. B **612**, 223 (2005) [hep-ph/0502063] and Nucl. Phys. B **724** (2005) 247 [hep-ph/0505042].
- [29] A. Denner, S. Dittmaier, M. Roth and D. Wackeroth, Nucl. Phys. B **560** (1999) 33 [hep-ph/9904472].
- [30] A. Denner and S. Dittmaier, Nucl. Phys. B **658** (2003) 175 [hep-ph/0212259].
- [31] A. Denner and S. Dittmaier, Nucl. Phys. B **734** (2006) 62 [hep-ph/0509141].
- [32] S. Dittmaier, Nucl. Phys. B **565** (2000) 69 [hep-ph/9904440].
- [33] A. Bredenstein, S. Dittmaier and M. Roth, Eur. Phys. J. C **44** (2005) 27 [hep-ph/0506005].
- [34] A. Denner, Fortsch. Phys. **41** (1993) 307.
- [35] A. Denner, S. Dittmaier, and G. Weiglein Nucl. Phys. B **440** (1995) 95 [hep-ph/9410338].
- [36] S. Dittmaier, Phys. Rev. D **59** (1999) 016007 [hep-ph/9805445].
- [37] W. F. L. Hollik, Fortsch. Phys. **38** (1990) 165.



- [38] J. Küblbeck, M. Böhm and A. Denner, Comput. Phys. Commun. **60** (1990) 165;  
H. Eck and J. Küblbeck, *Guide to FeynArts 1.0*, University of Würzburg, 1992.
- [39] T. Hahn, Comput. Phys. Commun. **140** (2001) 418 [hep-ph/0012260].
- [40] T. Hahn and M. Perez-Victoria, Comput. Phys. Commun. **118** (1999) 153  
[hep-ph/9807565];  
T. Hahn, Nucl. Phys. Proc. Suppl. **89** (2000) 231 [hep-ph/0005029].
- [41] M. W. Grünewald *et al.*, in *Reports of the Working Groups on Precision Calculations for LEP2 Physics*, eds. S. Jadach, G. Passarino and R. Pittau (CERN 2000-009, Geneva, 2000), p. 1 [hep-ph/0005309].
- [42] G. 't Hooft and M. Veltman, Nucl. Phys. B **153** (1979) 365.
- [43] W. Beenakker and A. Denner, Nucl. Phys. B **338** (1990) 349.
- [44] A. Denner, U. Nierste and R. Scharf, Nucl. Phys. B **367** (1991) 637.
- [45] G. Passarino and M. Veltman, Nucl. Phys. B **160** (1979) 151.
- [46] A. Sirlin, Phys. Rev. D **22** (1980) 971.
- [47] T. Stelzer and W.F. Long, Comput. Phys. Commun. **81** (1994) 357 [hep-ph/9401258].
- [48] T. Kinoshita, J. Math. Phys. **3** (1962) 650;  
T. D. Lee and M. Nauenberg, Phys. Rev. **133** (1964) B1549.
- [49] E. A. Kuraev and V. S. Fadin, Sov. J. Nucl. Phys. **41** (1985) 466 [Yad. Fiz. **41** (1985) 733];  
G. Altarelli and G. Martinelli, in *Physics at LEP*, eds. J. Ellis and R. Peccei, (CERN 86-02, Geneva, 1986), Vol. 1, p. 47;  
O. Nicosini and L. Trentadue, Phys. Lett. B **196** (1987) 551 and Z. Phys. C **39** (1988) 479;  
F. A. Berends, W. L. van Neerven and G. J. H. Burgers, Nucl. Phys. B **297** (1988) 429 [Erratum-ibid. B **304** (1988) 921].
- [50] W. Beenakker *et al.*, in *Physics at LEP2* (Report CERN 96-01, Geneva, 1996), eds. A. Altarelli, T. Sjöstrand and F. Zwirner, Vol. 1, p.3, hep-ph/9602351.
- [51] F. A. Berends, R. Pittau and R. Kleiss, Nucl. Phys. B **424** (1994) 308 [hep-ph/9404313] and Comput. Phys. Commun. **85** (1995) 437 [hep-ph/9409326];  
F. A. Berends, P. H. Daverveldt and R. Kleiss, Nucl. Phys. B **253** (1985) 441;  
J. Hilgart, R. Kleiss and F. Le Diberder, Comput. Phys. Commun. **75** (1993) 191.
- [52] A. Denner, S. Dittmaier, M. Roth and D. Wackeroth, Comput. Phys. Commun. **153**, 462 (2003) [hep-ph/0209330].
- [53] A. Bredenstein, S. Dittmaier and M. Roth, Eur. Phys. J. C **36** (2004) 341 [hep-ph/0405169].

- [54] G.P. Lepage, J. Comput. Phys. **27** (1978) 192.
- [55] V. S. Fadin, V. A. Khoze and A. D. Martin, Phys. Lett. B **311** (1993) 311;  
D. Y. Bardin, W. Beenakker and A. Denner, Phys. Lett. B **317** (1993) 213.
- [56] S. Eidelman *et al.* [Particle Data Group Collaboration], Phys. Lett. B **592** (2004) 1.
- [57] F. Jegerlehner, hep-ph/0105283.
- [58] D. Y. Bardin, A. Leike, T. Riemann and M. Sachwitz, Phys. Lett. B **206** (1988) 539;  
D. Wackeroth and W. Hollik, Phys. Rev. D **55** (1997) 6788 [hep-ph/9606398];  
W. Beenakker *et al.*, Nucl. Phys. B **500** (1997) 255 [hep-ph/9612260].
- [59] A. Denner, S. Dittmaier, M. Roth and D. Wackeroth, Nucl. Phys. B **587** (2000) 67  
[hep-ph/0006307].
- [60] W. Beenakker, F. A. Berends and A. P. Chapovsky, Nucl. Phys. B **548** (1999) 3  
[hep-ph/9811481].